



<https://theses.gla.ac.uk/>

Theses Digitisation:

<https://www.gla.ac.uk/myglasgow/research/enlighten/theses/digitisation/>

This is a digitised version of the original print thesis.

Copyright and moral rights for this work are retained by the author

A copy can be downloaded for personal non-commercial research or study,
without prior permission or charge

This work cannot be reproduced or quoted extensively from without first
obtaining permission in writing from the author

The content must not be changed in any way or sold commercially in any
format or medium without the formal permission of the author

When referring to this work, full bibliographic details including the author,
title, awarding institution and date of the thesis must be given

Enlighten: Theses

<https://theses.gla.ac.uk/>
research-enlighten@glasgow.ac.uk

Technology development of 3-D GaAs radiation detectors

Andrew R. Meikle

**Faculty of Engineering
University of Glasgow**

*Thesis submitted for the degree of
Master of Science*

October 1999

© A. R. Meikle 1999

ProQuest Number: 10644193

All rights reserved

INFORMATION TO ALL USERS

The quality of this reproduction is dependent upon the quality of the copy submitted.

In the unlikely event that the author did not send a complete manuscript and there are missing pages, these will be noted. Also, if material had to be removed, a note will indicate the deletion.



ProQuest 10644193

Published by ProQuest LLC (2017). Copyright of the Dissertation is held by the Author.

All rights reserved.

This work is protected against unauthorized copying under Title 17, United States Code
Microform Edition © ProQuest LLC.

ProQuest LLC.
789 East Eisenhower Parkway
P.O. Box 1346
Ann Arbor, MI 48106 – 1346

GLASGOW
UNIVERSITY
LIBRARY

12022-COPY 2

Abstract

A novel type of GaAs radiation detector featuring a three-dimensional array of electrodes that penetrate through the detector bulk is described. The development of the technology to fabricate such a detector is presented along with electrical and radiation source tests. Simulations of the electrical characteristics are given for detectors of various dimensions.

Laser drilling was used to create holes in the detector bulk. Two types of laser were investigated: Nd:YAG and Ti: Sapphire. The Nd:YAG laser produced repeatable round holes of 30 μm diameter with little or no taper and smooth internal walls. The Ti:Sapphire laser produced holes of 100 μm diameter with very little ejected debris.

Electrodes were formed within the holes by metal evaporation, creating diode cells with a Schottky-Schottky configuration. Two types of cell were fabricated: three-electrode and nine-electrode. The cells had 60 μm diameter holes with a 210 μm pitch.

Electrical measurements made on both cells revealed characteristics with low leakage currents and high breakdown voltages. The three-electrode cell had a reverse breakdown voltage of approximately 100 V and a reverse leakage current of approximately 20 nA while the nine-electrode cell had a reverse breakdown voltage of approximately 500 V and a reverse leakage current of approximately 5 nA. Forward and reverse bias I-V measurements showed asymmetrical characteristics, which are not seen in planar diodes.

Energy spectra were obtained using 5.45 MeV alpha particles and 60 keV photons. The alpha source measurements produced a charge collection efficiency of 50%.

Simulations of a nine-electrode cell with identical dimensions to the fabricated cell were performed. The results showed asymmetrical forward and reverse bias I-V characteristics, similar to those found experimentally. The simulated I-V characteristics also showed a breakdown voltage of 500 V with low leakage currents, consistent with those found experimentally. The simulations showed that the cell is not fully depleted at 500 V. Simulations of a nine-electrode cell with 10 μm electrodes with a 25 μm pitch were also performed. The I-V characteristics again showed a high breakdown voltage with a low leakage current but also showed a full depletion voltage of just 8 V.

Contents

1	Introduction	1
1.1	Introduction	1
1.2	Planar semiconductor detectors	2
1.3	Gallium arsenide as a radiation detector material	3
1.4	GaAs radiation detector performance limitations.	4
1.5	3-D radiation detectors	4
2	Semiconductor theory	6
2.1	Introduction	7
2.2	Crystal structure	7
2.2.1	Valence bonds	8
2.2.2	Energy bands	9
2.2.3	Density of states and carrier concentration	12
2.3	Carrier transport	14
2.4	Schottky barrier diodes	17
2.4.1	Current transport in metal-semiconductor junctions	19
2.5	Interaction of radiation with semiconductor detectors	21
2.5.1	Charged particles	21
2.5.2	Photons	22
3	Fabrication development	23
3.1	Introduction	23
3.1.1	Material choice	23
3.1.2	Wafer treatment	24
3.2	Electrode fabrication	24
3.2.1	Laser drilling of holes	25
3.2.2	Hole analysis	27

3.2.3	Drilling damage	35
3.2.4	Resist spinning.	36
3.2.5	Wet chemical etching	37
3.2.6	Metal deposition	39
3.2.7	Wire bonding	39
3.2.8	Fabrication summary	40
4	Detector characterisation	42
4.1	Introduction..	42
4.2	Current-voltage characteristics.	42
4.2.1	Three-electrode cell	43
4.2.2	Nine-electrode cell	45
4.3	Charge collection	48
4.3.1	Alpha particle tests.	48
4.3.2	Gamma source tests	52
4.4	Simulated performance	53
4.4.1	Simulation cell 1.	54
4.4.2	Simulation cell 2.	57
5	Summary and conclusion	60
A	General properties of GaAs	64

List of figures

1.1 Basic planar detection operation.	3
1.2 3-D detection operation.	5
2.1 Basic cubic-crystal cells	7
2.2 GaAs crystal structure	7
2.3 Miller planes in a crystal.	8
2.4 Two-dimensional representation of a tetrahedron bond	8
2.5 Schematic energy band representations of (a) an insulator, (b) a semiconductor, and (c) conductors	9
2.6 The energy band structures in Si and GaAs	11
2.7 Carrier drift velocities in GaAs as a function of electric field	15
2.8 The formation of a barrier at a metal-semiconductor interface	18
2.9 Transport processes in a reverse biased Schottky barrier	20
3.1 Absorption depth vs wavelength.	24
3.2 Laser optic path	25
3.3 Holes drilled with a 15 cm focal length lens	26
3.4 Array of 30 μm diameter holes viewed with increasing magnification	27
3.5 30 mm diameter holes viewed at a 60 degree angle with increasing magnification from a to d.	28
3.6 Vertically cleaved holes drilled with a 5 cm focal length lens, 1 mm iris and given an extra 100 pulses after breakthrough	29
3.7 Exit holes on bottom of substrate	30
3.8 Hole drilled with an effective focal length of 2.5 cm	31

3.9 Holes drilled with Ti:Sapphire laser using a 15 cm focal length lens.	33
3.10 3-D detector fabrication process flow	39
4.1 Three-electrode test circuit	41
4.2 Three-electrode cell I-V characteristics	42
4.3 Three-electrode cell reverse bias characteristic	43
4.4 Nine-electrode cell test circuit	43
4.5 Nine-electrode cell I-V characteristic	44
4.6 Approximate electric field density for (a) nine-electrode cell and (b) three- electrode cell.	45
4.7 Alpha source test measurement apparatus	47
4.8 5.45 MeV α particle spectrum of nine-electrode cell at room temperature	49
4.9 CCE measurements of 5.45 MeV α particles at room temperature	50
4.10 60 keV γ - ray spectrum of nine-electrode cell at room temperature	51
4.11 Simulated nine-electrode cell reverse bias I-V characteristics	53
4.12 Simulated nine-electrode cell forward bias I-V characteristic	54
4.13 Simulated potential distribution across a nine-electrode 3D structure	55
4.14 Simulated potential distribution across Cell 2	56
4.15 Cell 2 reverse biased I-V characteristic	56
4.16 Depletion region across Cell 1 at 550 V.	57

Acknowledgements

I would like to thank a number of people for the help, support and encouragement I received throughout the duration of this work.

My supervisors, Ken Smith and John Marsh, kindly provided me with the opportunity to carry out this project. Their patient guidance and helpful advice at all times has been of most importance.

In the Detector Development Group lab, various members of staff and students have helped in the completion of this work. Richard Bates has been extremely helpful in discussing the measurements, making the general picture a good deal clearer, while Val O'Shea's kindly advice has prevented some potential pitfalls. Fred Doherty has been of great assistance in both the preparation of GaAs samples and measurement of radiation source tests. Keith Mathieson was very kind in running detector simulations while John Watt, Craig Whitehill, Steve Passmore, Derek Livingston and Stephen Bryce have all provided useful discussions at various times.

In the Laser Ionisation Group, Ken Ledingham and Tom McCanny were of invaluable assistance in the laser drilling of holes, as was Walter Perrie at BNFL.

The Solid State Physics group were very kind in allowing me to use their electron microscope to analyse the results of the laser drilling process.

The use of the fabrication facilities in the Dept. of Electrical and Electronic Engineering was essential and various members of staff there, too numerous to mention, were of great help.

Finally, I would like to make a special mention to the late Colin Raine. As a member of the interview panel that selected me for employment within the group, he helped give me the opportunity to carry out projects like the one described in this thesis. His kind manner, extensive knowledge and willingness to help others made for a happier working life in the group, where he is sadly missed.

I would like to dedicate this work to Jackie. My stubborn refusal to spell her name the way she prefers has now made it into print.

Chapter 1

Introduction

1.1 Introduction

In recent years there has been a surge of interest in the development of Gallium Arsenide (GaAs) radiation detectors. The fields of High Energy Physics (H.E.P.) and X-ray imaging have seen much of this work, with extensive research being carried out on material characterisation and design improvements. The vast majority of the detectors used for this research consisted of bulk-grown semi-insulating undoped GaAs (SI-U GaAs) with planar contacts on the material surface, making both their fabrication and operation simple. Unfortunately, under certain conditions, these detectors were found to be limited in their performance: a large number of native defects are present which result in incomplete charge collection. Voltages in the region of $1 \text{ V}/\mu\text{m}$ are needed to deplete the detector bulk that, normally, is hundreds of microns thick. Typical drift paths for ionisation charges are at least comparable to that thickness, collection times are limited by this thickness and charge collection efficiency is greatly reduced under high radiation loads due to the drift distance being reduced because of bulk damage.

A novel architecture that uses a three-dimensional array of electrodes that penetrate all the way through the thickness of the detector bulk offers the possibility of overcoming these limitations. With pitches as small as $25 \mu\text{m}$, the advantages of such a structure include short collection distances, fast collection times and low depletion voltages.

The aim of this thesis is to develop the technology to create a three-dimensional detector and to evaluate its operational characteristics. This chapter continues with a brief history of semiconductor radiation detectors and the planar technique, followed by the motivation for developing GaAs as a suitable detector material and its proposed uses. The limitations on its operation, briefly mentioned above, are discussed in

greater detail and the chapter concludes with a proposal for the new detector architecture. Semiconductor and Schottky barrier theories are explained in chapter 2 while chapter 3 describes the technology development and fabrication of three-dimensional detectors. Chapter 4 presents the results of the electrical and radioactive source measurements along with detector simulations and chapter 5 presents the conclusions and suggestions for future work.

1.2 Planar semiconductor detectors

The first solid state radiation detector was fabricated in 1945 by Van Heerden, who showed alpha particle and gamma ray detection with AgCl crystals [1]. Following this breakthrough, the development of semiconductor radiation detectors took off, and although they quickly met with much scepticism due to the difficult problems imposed on their operation by charge carrier trapping and space-charge accumulation [2,3], great success came in the 1960's with the development of high purity, planarised Ge and Si spectrometers [4]. Since then, planar semiconductor radiation detectors have been used in a variety of applications. For example, the introduction of the planar technique [5] in 1980 for the fabrication of large-scale silicon detectors enabled position measurements to be carried out with semiconductors for H.E.P. experiments. Since then, the use of planar semiconductor detectors for tracking and vertexing has been extensive, with microstrip vertex detectors being used in H.E.P. experiments throughout the world.

A planar semiconductor detector is operated by applying a voltage across contacts positioned on opposite sides of the device. Ionizing radiation (for instance, gamma rays or charged particles) absorbed in the material excites electron-hole pairs in proportion to the energy deposited in the detector (Fig.1). These free charges then drift through the device bulk under the influence of an applied electric field, creating an induced charge at the terminals of the device proportional to the distance travelled by the charge carriers (both electrons and holes) through the applied electric field. It is this induced charge that is measured to determine the energy of the absorbed radiation. The general relationship for the change in induced charge at the detector contacts is described by the Shockley-Ramo theorem [6,7], in which

$$dQ^* = \frac{qN_0}{W} dx \quad (1.1)$$

where Q^* is the induced charge, q is the electronic charge, N_0 is the initial number of electron-hole pairs and W is the detector width. In an ideal, trap-free semiconductor material, full charge carrier collection at the electrodes is possible and the total induced charge is simply

$$Q^* = qN_0.$$

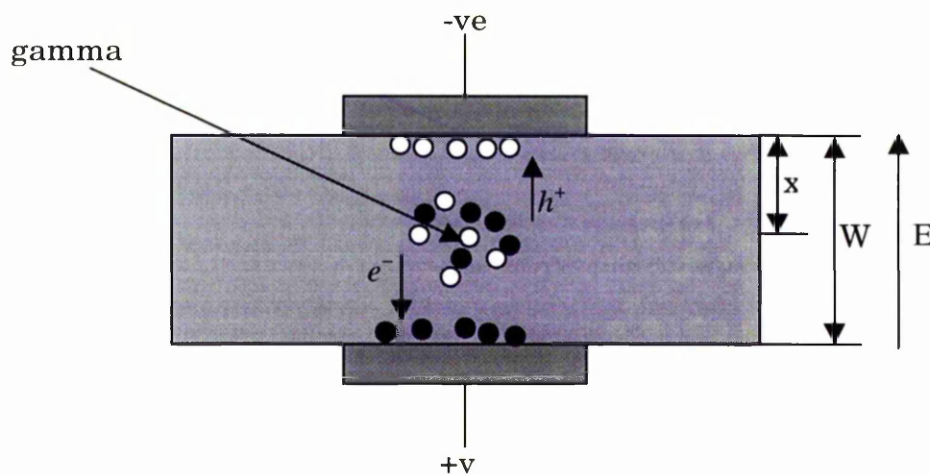


Fig. 1.1 Basic planar detection operation, in which charge carriers excited at location x by a quantum of radiation are separated by an electric field and swept to opposite contacts of the device. The gamma ray passes through the material and any energy deposited in the depleted volume can be detected. The signal measured is from the induced charge produced by the motion of the carriers as they move through the electric field and not the charge of the “collected” electrons and holes.

1.3 GaAs as a radiation detector material

Semiconductor radiation detectors operated at room temperature require relatively large bandgap energies to minimise the thermal generation of charge carriers. They should also have a relatively large atomic number to increase X-ray and gamma ray interaction probability. High charge carrier mobilities and long charge carrier lifetimes, which can offer high-speed particle detection and signal processing, are desirable features in detector materials.

GaAs is a semiconductor with many features which make it suitable for room temperature operation, including a moderately wide band gap (1.424 eV at 300 K), relatively high charge carrier mobility (nearly six times greater than that of silicon) and an average atomic number of 32. GaAs has been studied as a radiation detector material since the early 1960's [8,9], with crystal growth and fabrication technologies progressing significantly since then as a direct result of efforts in the VLSI industry. A variety of applications for bulk GaAs radiation detection devices has been reported, including particle detection for H.E.P. [10-15], radiation dose monitoring through nuclear displacement [16], pixel arrays for X-ray imaging [17], pixel arrays for thermal neutron imaging [18] and high-speed radiation pulse detection [19].

1.4 GaAs radiation detector performance limitations

H.E.P. radiation hardness studies [20, 21] have shown, however, that high radiation doses introduce deep level defects to the bulk which affect the main parameters of planar GaAs detectors, namely the leakage current density, mean free drift length and charge collection efficiency. Tests on 200 μm thick circular pad diodes before and after irradiation by 1 MeV/c neutrons, 24 GeV/c protons and 300 MeV/c pions were carried out to determine the radiation hardness of GaAs. For a charged particle fluence of 2×10^{14} p/cm², the charge collection efficiency dropped to approximately 25% of its pre-irradiation level while the leakage current density increased to approximately 2-3 times its pre-irradiation level due to a reduction in Schottky barrier height [20]. A more systematic study gives an insight into why there is such a large loss of charge: for an equivalent neutron fluence of 1.3×10^{15} p/cm², the mean free drift length for both electrons and holes decreases dramatically, down to approximately 30-40 μm for electrons and approximately 20-30 μm for holes [21]. These reduced drift lengths will cause incomplete charge collection in a 200 μm thick detector.

1.5 3-D radiation detectors

The obvious way to overcome this charge collection problem would be to fabricate a planar detector on a thin, say 25 μm , sample of GaAs. This would enable the majority of the charge to be collected, as the reduced carrier drift length would be sufficient for charge carriers to reach the electrodes. Unfortunately, the brittle nature of GaAs would make the fabrication of such a device impractical. Also, radiation detectors,

especially X-ray detectors, are normally required to be hundreds of microns thick in order to maximise their absorption efficiency. One way of creating such a detector, proposed by Parker et al, [22] has thin cylindrical electrodes with 25 μm of material between contacts that penetrate some or all of the way through the detector bulk. These cylindrical electrodes are biased to create an electric field that sweeps the electron and hole charge carriers laterally through the bulk for collection at oppositely biased electrodes, and charge collection will take place throughout the thickness of the bulk. The electrode pitch would be sufficiently small to collect the majority of the charge after irradiation and the need for a detector bulk hundreds of microns thick would be satisfied. Other promising features of this type of detector include fast collection times and low depletion voltages. Figure 1.2 shows a cross-section of such a detector.

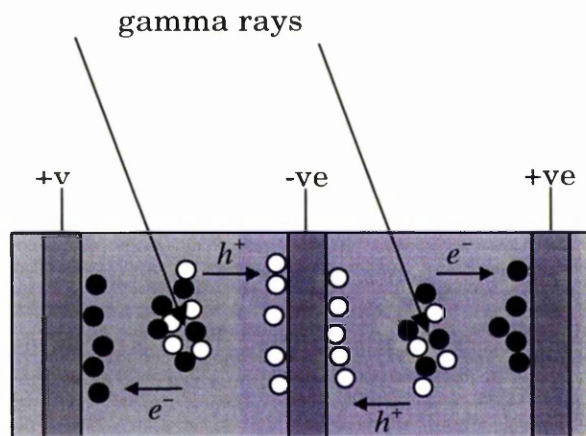


Fig. 1.2 3-D detection operation, where a central electrode is surrounded by opposite polarity electrodes. The charge carriers are swept laterally through the bulk and are collected at the electrodes throughout the thickness of the bulk.

The possibility exists to utilise 3-D detectors for various applications. Fabrication steps following large-scale electrode formation could be varied to produce monolithic pixel detectors [23], bump-bonded pixel detectors [24] and strip detectors. Therefore, both the fields of H.E.P. and X-ray imaging could benefit from this type of detector.

Chapter 2

Semiconductor theory

2.1 Introduction

In order to understand fully the operation of detectors based on GaAs, a description of the basic properties of semiconductors is given. A description of the Schottky barrier diode is then given since this type of diode is found in this work. Throughout the chapter, references will be made to the properties of GaAs and, where appropriate, a comparison between GaAs and silicon will be made.

Solid-state materials can be grouped into three classes - insulators, semiconductors and conductors. Insulators such as fused quartz and glass have very low conductivities, in the order of 10^{-18} to 10^{-8} S/cm; conductors such as aluminium and silver have high conductivities, typically from 10^4 to 10^6 S/cm. Semiconductors have conductivities between those of insulators and those of conductors. The conductivity of a semiconductor is generally sensitive to temperature, illumination, magnetic field and minute amounts of impurity atoms. This sensitivity in conductivity makes the semiconductor one of the most important materials for electronic applications.

2.2 Crystal Structure

Single crystal semiconductor materials have atoms arranged in a three-dimensional periodic fashion. The periodic arrangement of atoms in a crystal is called a lattice. For a given semiconductor, there is a unit cell that is representative of the entire lattice.

Figure 2.1 shows some basic cubic-crystal unit cells. The simple cubic crystal (a) has atoms occupying each corner of the cubic lattice. It has six nearest-neighbour atoms at equal distances. The body-centered cubic crystal (b) has an atom located in the centre of the cube in addition to the eight corner atoms and has eight nearest-neighbour atoms. The face-centered cubic crystal (c) has one atom at each of the

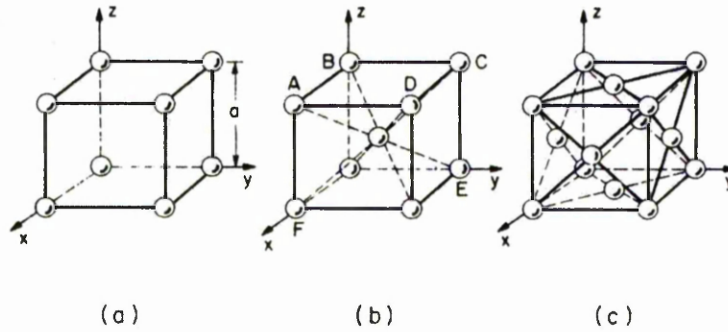


Fig. 2.1 Basic cubic-crystal

six cubic faces in addition to the eight corner atoms and has twelve nearest-neighbour atoms.

However, the commonly used semiconductors have more complex cubic structures. The elemental semiconductors, silicon and germanium, have a diamond lattice structure, where each atom is surrounded by four equidistant neighbours. The III-V compound semiconductor, GaAs, has a zincblende structure (Fig. 2.2), which is similar to the diamond lattice. Both these structures can be seen as two interpenetrating face-centred cubic lattices, the difference being that, in GaAs, one lattice has Gallium (column III) atoms and the other has Arsenic (column V) atoms.

For most of the cubic structures shown in Fig.2.1, it can be seen that some crystal planes have a different number of atoms to others and that the atomic spacing is also different. Therefore, the crystal properties along different planes are different, and the electrical and other device characteristics are dependent on the crystal orientation. The

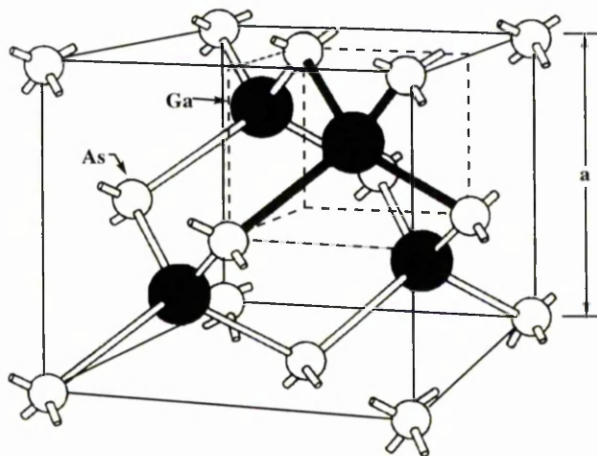


Fig. 2.2 GaAs crystal

various planes in a crystal can be defined by using Miller indices. These are obtained by finding the intercepts of the plane on the three Cartesian coordinates in terms of the lattice constant and then taking the reciprocals of these numbers and reducing them to the smallest three integers with the same ratio. Figure 2.3 shows some Miller indices of cubic crystal planes.

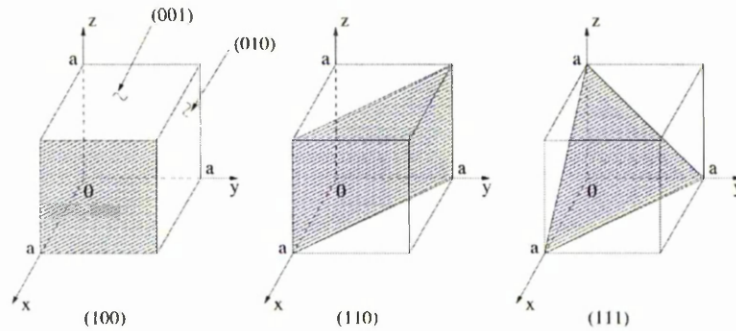


Fig. 2.3 Miller planes in a

2.2.1 Valence Bonds

In a diamond lattice, each atom is surrounded by four nearest neighbours. Figure 2.4 shows a simplified two-dimensional bonding diagram for this tetrahedron configuration. Each atom has four electrons in the outer orbit, and each atom shares these valence electrons with its four neighbours. This sharing of electrons is known as covalent bonding; each electron pair constitutes a covalent bond. Covalent bonding occurs between atoms of the same element or between atoms of different elements that have similar outer-shell electron configurations. The force of attraction for the electrons by both nuclei holds the two atoms together. For a zincblende atom such as

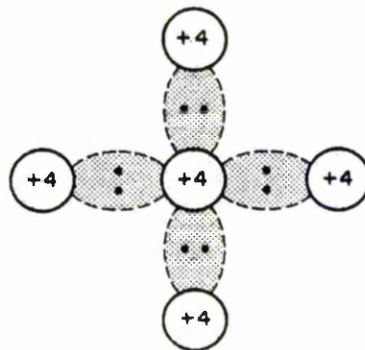


Fig. 2.4 Two-dimensional representation of a

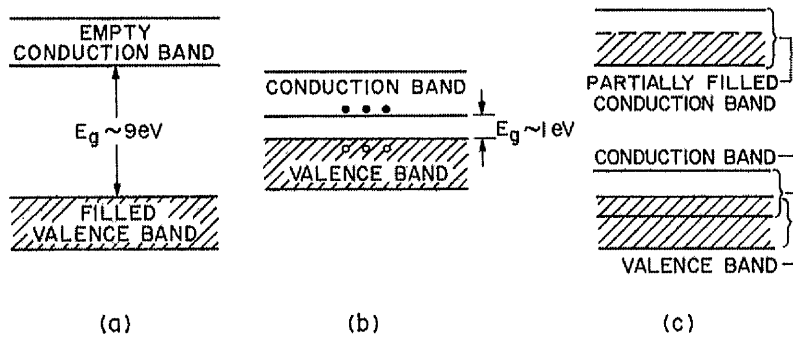


Fig. 2.5 Schematic energy band representations of (a) an insulator, (b) a semiconductor, and (c) conductors.

GaAs, the major bonding force is from the covalent bonds. However, GaAs has a slight ionic bonding force, that is, an electrostatic attractive force between each Ga^- ion and its four neighbouring As^+ ions, or between each As^+ ion and its four neighbouring Ga^- ions.

Covalent bonds may be broken by thermal excitation. When this happens, the resulting free electron can participate in current conduction. The resulting electron deficiency in the bond may be filled by a neighbouring electron, which results in a shift of the deficiency location. Thus, we may consider this mobile deficiency as a particle similar to an electron, which is able to contribute to the conductivity. This particle is called a hole. It carries a positive charge and moves, under the influence of an electric field, in the direction opposite to that of an electron.

2.2.2 Energy Bands

For an isolated atom, the electrons of the atom can only have discrete energy levels. However, in a crystal lattice, where many atoms are brought close together, the energy levels split into separate but closely spaced levels due to atomic interaction. This results in an essentially continuous band of energy. When the distance between atoms approaches the equilibrium inter-atomic spacing of the lattice, this band splits into two bands. These bands are separated by a region called the forbidden gap, or bandgap, of width E_g , where there are no allowed energy levels for electrons. The upper band is called the conduction band, while the lower band is called the valence band. Electrons in the conduction band can move freely inside the crystal and thus directly conduct

current. The valence band electrons are participating in atomic bonds and thus are bound to atoms in the crystal lattice.

Figure 2.5 shows the energy band diagrams of three classes of solids - insulators, semiconductors and conductors. In an insulator, the valence electrons form strong bonds between neighbouring atoms. These bonds are difficult to break, and consequently there are no free electrons to participate in current conduction. Electrons occupy the valence band energy levels while the conduction band levels are all empty. The bandgap is large and thermal energy or an applied electric field cannot raise the uppermost electron in the valence band to the conduction band.

In a semiconductor, the bonds between neighbouring atoms are only moderately strong. Therefore, thermal vibrations will break some bonds. When this happens, a free electron along with a free hole results. The bandgap of a semiconductor is not as large as that of an insulator and, because of this, some electrons will be able to move from the valence band to the conduction band, leaving holes in the valence band. When an electric field is applied, both the electrons in the conduction band and holes in the valence band will gain kinetic energy and conduct electricity.

In conductors, the conduction band either is partially filled or overlaps the valence band so that there is no bandgap. As a consequence, the uppermost electrons in the partially filled band or electrons at the top of the valence band can move to the next-higher available energy level when they gain kinetic energy. Therefore, current conduction can readily occur in conductors.

The most important parameter in semiconductor physics is the bandgap, Eg. The energy band diagram of Fig. 2.5 is a simplified representation of a rather complex energy band structure. Figure 2.6 shows slightly more complicated energy band diagrams for silicon and GaAs in which the energy is plotted against the carrier momentum in the crystal for two crystal directions. At room temperature and under normal atmosphere, the values of the bandgap are 1.12 eV for silicon and 1.42 eV for GaAs.

This should result in a lower number of thermally generated carriers in GaAs than in silicon at a given temperature. Another important difference is that, for GaAs, the maximum in the valence band and the minimum in the conduction band occur at the same carrier momentum ($p = 0$).

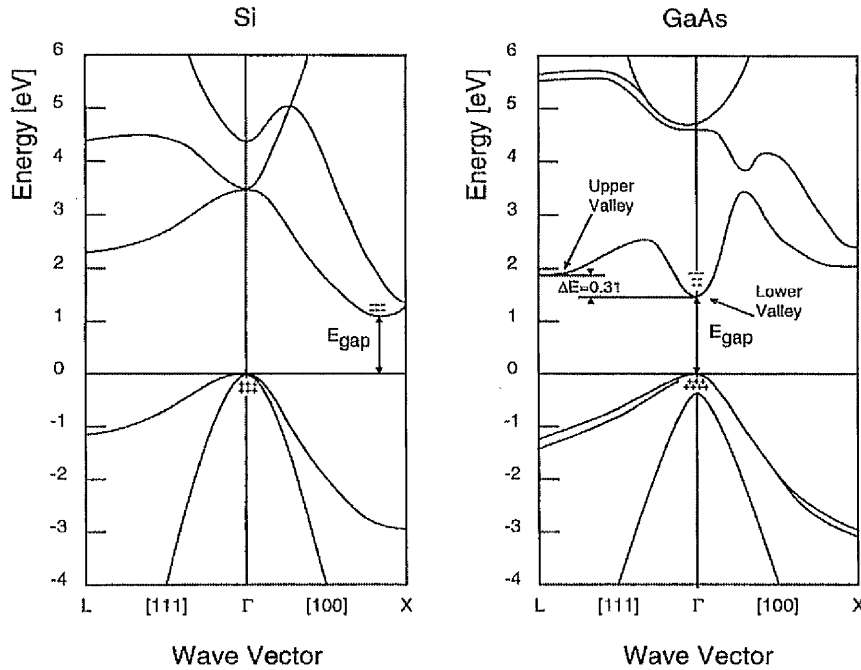


Fig. 2.6 The energy band structure in Si

Thus, an electron making a transition from the valence band to the conduction band can do so without a change in p value. However, in silicon, an electron making the same transition requires a change in momentum as well as a change in energy. Because of this, GaAs is called a direct semiconductor and silicon is called an indirect semiconductor. Spontaneous emission or absorption of a photon can accompany electron transitions in direct semiconductors and are very important for light-emitting diodes and semiconductor lasers.

For a free electron, the kinetic energy E is given by

$$E = \frac{p^2}{2m_0} \quad (2.1)$$

where p is the particle momentum and m_0 is the free-electron mass. However, because of the periodic potential in the lattice, the carriers in a semiconductor are not free particles and the effective mass of a conduction electron is usually less than the mass of a free electron, sometimes much less. The energy momentum relationship of a conduction electron can be written as

$$E = \frac{p^2}{2m_n} \quad (2.2)$$

where p is the electron momentum and m_n is the electron effective mass. The concept of effective mass is very useful as it enables us to treat holes and electrons essentially as classical charged particles.

2.2.3 Density of states and carrier concentration

We can put more detail into our picture of semiconductors by describing the number of electrons at each energy. At finite temperatures, continuous thermal agitation results in the excitation of electrons from the valence band to the conduction band and leaves an equal number of holes in the valence band. The electron density $n(E)$ in the conduction band is given by the product of the density of energy states ($N(E)$) in this band and the probability of those states being occupied by electrons $F(E)$. Thus, the electron density in the conduction band is given by integrating $N(E) F(E) dE$ from the bottom of the conduction band to the top of the conduction band.

The probability that an electron occupies an electronic state with energy E is given by the Fermi-Dirac distribution function

$$f(E) = \frac{1}{1 + \exp\left(\frac{E - E_F}{k_B T}\right)} \quad (2.3)$$

where k_B is the Boltzmann constant, T is the absolute temperature in Kelvin, and E_F is the Fermi level. The Fermi level is the energy at which the probability of occupation by an electron is exactly one half.

For a non-degenerate semiconductor ($E_v < E_F < E_c$), the electron density n in the conduction band is given as

$$N_C \exp\left(-\frac{E_C - E_F}{k_B T}\right) \quad (2.4)$$

and

$$N_C = 2 \left(\frac{2\pi m_n^* k_B T}{\hbar^2} \right)^{3/2} \quad (2.5)$$

where N_c is the effective density of states in the conduction band.

The hole density p in the valence band is given as

$$N_v \exp\left(-\frac{E_F - E_v}{k_B T}\right) \quad (2.6)$$

and

$$N_v = 2 \left(\frac{2\pi m_p^* k_B T}{\hbar^2} \right)^{3/2} \quad (2.7)$$

where N_v is the effective density of states in the valence band.

For an intrinsic semiconductor, the number of electrons per unit volume in the conduction band is equal to the number of holes per unit volume in the valence band, that is $n = p = n_i$. The intrinsic carrier density is given as

$$pn = n_i^2 \quad (2.8)$$

and

$$n_i^2 = N_c N_v \exp\left(-\frac{E_g}{k_B T}\right) \quad (2.9)$$

$$n_i = \sqrt{N_c N_v} \exp\left(-\frac{E_g}{2k_B T}\right) \quad (2.10)$$

where $E_g = (E_c - E_v)$. Equation 2.8 is called the mass action law and is valid for both intrinsic and extrinsic (i.e., doped with impurities) semiconductors under a thermal equilibrium condition.

A semiconductor becomes extrinsic when it is doped with impurities and impurity energy levels are introduced. As a result the relative carrier concentrations in the bands change. There are two kinds of dopant, donors and acceptors.

The extra electron attached to a donor can be liberated by a small amount of energy, 10-50 meV, so that at room temperature, where $kT \sim 25$ meV the electron is free to travel through the whole crystal and contribute to an increased conductivity. Acceptors remove an electron from the valence band, leaving a mobile hole. If both donors and acceptors are added to the same crystal, their effects cancel – only the

excess of one above the other has an effect on the free carrier densities. The changes in the concentration in an extrinsic semiconductor can be viewed in an energy band diagram as a shift of the Fermi level towards the band that has the majority of the carriers.

2.3 Carrier transport

Following on from the description of charge carriers in a semiconductor, we now consider various transport phenomena that arise from the motion of these carriers in semiconductors under the influence of an electric field and a carrier concentration gradient.

Electrons in the conduction band have a random thermal velocity, v_{th} , given by:

$$\frac{1}{2}m_n^*v_{th}^2 = \frac{3}{2}k_B T \quad (2.11)$$

At room temperature the electron thermal velocity is of the order of 10^4 ms^{-1} . A corresponding relationship also applies for holes.

Under the application of an external electric field (E) a drift component is added to the carrier velocity. The low field drift velocities for electrons (v_n) and holes (v_p) are

$$v_n = -\mu_n E \quad (2.12)$$

$$v_p = \mu_p E \quad (2.13)$$

where the constants of proportionality are the mobilities (μ_n, μ_p) of the carriers, which are carrier, temperature and material dependent. The drift velocity gives rise to a drift current density (J)

$$J = nqv = nq\mu E \quad (2.14)$$

The mobility depends on the effective mass and temperature of the carrier. With decreasing mass the mobility increases, thus, in GaAs, electrons have a much higher mobility than holes. For high electric fields (above 10^4 V/cm), the above relationships

are no longer valid as the mobilities are affected by the transfer of electrons into the upper valley in the conduction band (see Fig. 2.6). Electrons in the direct band, lower valley, have very high mobilities ($8500 \text{ cm}^2 \text{ V}^{-1} \text{ s}^{-1}$ at 300 K) resulting in velocities as high as $2 \times 10^7 \text{ cm/s}$ at an electric field of $3 \times 10^3 \text{ V/cm}$. As the electric field increases, the electrons are scattered into the indirect upper valley where the mobility is reduced due to the increase in effective mass. As a result, the average group velocity of the electrons begins to fall as the population of electrons in the upper valley rises. The drift velocity as a function of electric field for the carriers in GaAs is shown in Fig. 2.7.

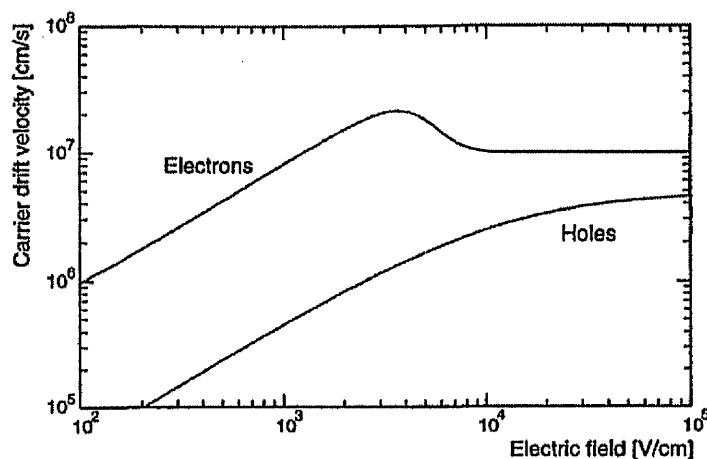


Fig. 2.7 Carrier drift velocities in GaAs as a function of

The resistivity (ρ) of a semiconductor is defined as the proportionality constant between the electric field and the drift current density, which at low fields depends on the mobility of the carriers:

$$\rho = \frac{E}{J} = \frac{1}{q(n\mu_n + p\mu_p)} \quad (2.15)$$

The conductivity (σ) of the sample is defined as the reciprocal of the resistivity:

$$\sigma = q(n\mu_n + p\mu_p) \quad (2.16)$$

Carriers in a semiconductor diffuse as well as drift. The carriers diffuse with a flux that is proportional to the carrier concentration gradient, and as the current density is simply the flux of carriers multiplied by the electron charge (q), then the diffusion currents are:

$$J_n = qD_n \frac{dn}{dx} \quad (2.17)$$

and

$$J_p = -qD_p \frac{dp}{dx} \quad (2.18)$$

where D_n and D_p are the diffusion coefficients for electrons and holes respectively.

The diffusion of electrons results in a change in the carrier concentration and therefore the electric field distribution will be altered. The movement of charge from point A to B due to diffusion will create an electric field that will oppose this motion and tend to cause electrons to drift from B to A. In equilibrium these balance

$$J_{drift} = J_{diffusion} \rightarrow qn\mu_n E_x = qD_n \frac{dn}{dx} \quad (2.19)$$

If the concentration gradient is described by:

$$n = n_0 \exp\left(\frac{qV}{k_B T}\right) \quad (2.20)$$

as it often is, then Einstein's relationship between the mobility and diffusion follow:

$$D_n = \left(\frac{k_B T}{q}\right) \mu_n \quad (2.21)$$

$$D_p = \left(\frac{k_B T}{q}\right) \mu_p \quad (2.22)$$

2.4 Schottky barrier diodes

A Schottky barrier may be created at the interface of a metal and a semiconductor when they are brought together and make contact [47]. The resultant rectifying phenomenon depends on the work functions (ϕ , the energy necessary to remove an electron from a material) of the two materials, assuming that surface states do not play a dominant part.

A semiconductor has an electron affinity (χ_s) which is the difference in energy between the bottom of the conduction band and the vacuum state. For a semiconductor in which the bands are flat, that is, without the presence of any electric fields, the work function (ϕ_s) and the electron affinity are related by

$$q\Phi_s = q(\chi_s + V_n) \quad (2.23)$$

where qV_n is the energy difference between E_c and E_v .

To understand the formation of a barrier we examine a metal of work function ϕ_m being brought into intimate contact with an n-type semiconductor of work function ϕ_s . The situation is illustrated in Fig. 2.8 for successively smaller separation distances, δ . (Note that in this case we have assumed that $\phi_m > \phi_s$). There will be a finite probability of electrons from the semiconductor penetrating the barrier and entering the metal, and this probability will increase as δ is decreased. These electrons departing from the semiconductor leave behind them positively charged ions, which results in a field across the junction in such a direction as to oppose the further transport across the junction. A state of equilibrium is set up, in the limit of $\delta \rightarrow 0$, in which the net transport of charge across the junction is reduced to zero. Thus, there is a potential barrier set up across the junction, which in this case is simply equal to the difference in the work functions of the materials ($\phi_m - \phi_s$). The expression for the barrier height is given by

$$q\Phi_{Bn} = q(\Phi_m - \chi) \quad (2.24)$$

The positively charged region in the semiconductor is depleted of charge carriers and is therefore called the depletion region. The two Fermi levels will line up,

resulting in band bending in the semiconductor as its Fermi level has changed position relative to the bands.

The metal semiconductor rectifier junction produced in this way has a current-voltage dependence similar to the more common p-n junction, forward bias being defined when the metal is made positive with respect to the semiconductor.

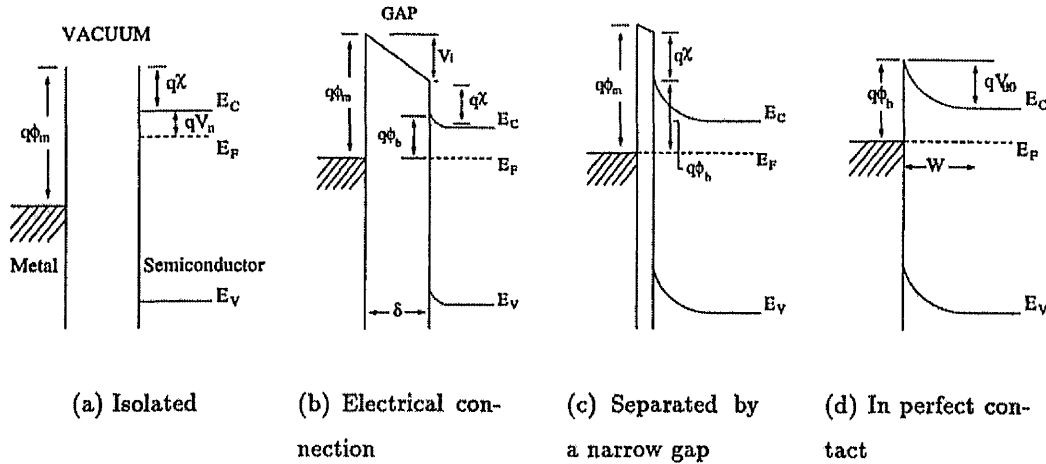


Fig. 2.8 Formation of a barrier at a metal-semiconductor interfaces.

By extension of the above explanation, the production of non-rectifying contacts would appear to be simply a matter of ensuring that $\phi_s > \phi_m$; no potential barrier would be set up and the junction would exhibit a linear (ohmic) I-V characteristic. Experimentally it is found that this is not necessarily the case. The density of surface states and a thin insulating layer between the metal and semiconductor may be such that the properties of the semiconductor surface and not the metal work function can be the dominant factor when producing a non-rectifying contact. Therefore, the mechanical/chemical treatment of the surface becomes very important. The same argument applies to the production of rectifying contacts. If the surface state density becomes very large, it can be shown that

$$q\Phi_{Bn} = qE_g - q\Phi_0 \tag{2.25}$$

where E_g denotes the semiconductor bandgap and Φ_0 is the neutral level, defined as the energy up to which all surface states are occupied with electrons at the electrically

neutral semiconductor surface [25]. In this case, the barrier height is completely independent of the choice of metal.

2.4.1 Current transport in metal-semiconductor junctions

Schottky diodes, when used as particle detectors, are operated under reverse bias to increase the high field region throughout the detector. Therefore a description of the current transport mechanisms of Schottky diodes under reverse bias will be presented.

The various ways in which electrons can be transported across a metal-semiconductor junction under reverse bias are shown schematically for an n-type semiconductor in Fig.2.9.

The mechanisms are:

- 1) Electron emission from the metal over the top of the barrier into the semiconductor: two processes exist – thermionic and diffusion. These are the dominant processes for Schottky barriers formed on moderately ($N_D < 10^{17} \text{ cm}^{-3}$) doped semiconductors at room temperature [26]. Schottky contacts in which the current transport mechanisms are mainly due to these processes, are referred to as ideal.
- 2) Quantum-mechanical tunnelling through the barrier: this process strongly depends on the barrier width. Therefore, current flow for heavily doped semiconductors, or those operated at low temperatures, will be dominated by this process.
- 3) Charge carrier generation in the space charge region: This process is due to the presence of generation-recombination centres within the space charge region, or, for low bandgap materials, due to band-to-band processes. These processes will be important for high barrier, low bandgap and low lifetime semiconductors.

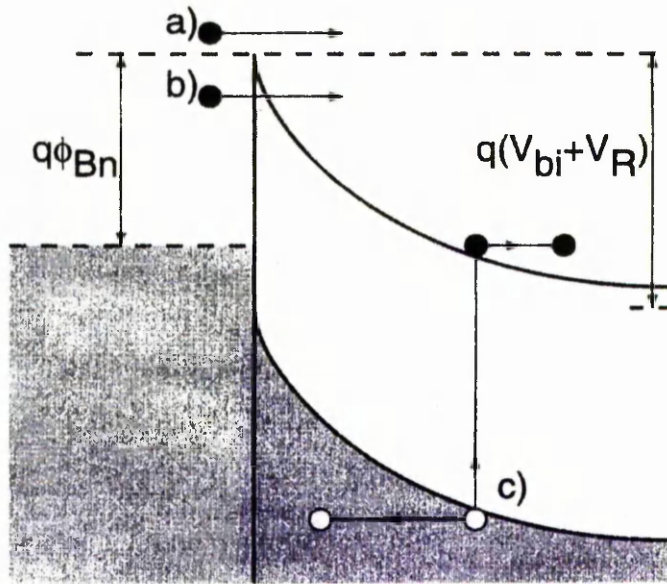


Fig. 2.9 Transport processes in a reverse biased Schottky barrier.

The current density for an ideal Schottky junction on an n-type semiconductor is derived from a combination of the thermionic emission and diffusion emission processes and is given by

$$J = A^{**} T^2 \exp\left(-\frac{\Phi_{Bn}}{k_B T}\right) \left[\exp\left(-\frac{q(V_{bi} + V_R)}{k_B T}\right) - 1 \right] \quad (2.26)$$

where

$$A^{**} = \frac{4\pi n_e^* q k_B^3}{h^3} \frac{1}{1 + v_R / v_D} \quad (2.27)$$

is the effective Richardson constant [26]. v_R and v_D denote the effective recombination and diffusion velocity, respectively.

For highly doped semiconductors at high reverse biases, the leakage current density is increased by the Schottky effect. This effect is the image-force induced lowering of the potential energy for a charge carrier emission when an electric field is applied.

2.5 Interaction of radiation with semiconductor detectors

Radiation passing through a semiconductor detector deposits energy along its trajectory through interaction with the detection medium. This energy creates electron-hole pairs along this trajectory and if an electric field is present these carriers will be swept to the contacts of the detector to create a current. This current can be amplified to form a signal that is proportional to the charge created in the active volume of the device.

Charged particles and photons react in different ways when interacting with matter. This difference will now be examined.

2.5.1 Charged particles

Charged particles interact with semiconductor material primarily through electromagnetic scattering by the electrons and nuclei in the atoms of the material. Inelastic scattering by electrons is the dominant mechanism as the mass of the nucleus is large in comparison to the mass of the particle. Although the amount of energy transferred in each collision is small, there are many such collisions per unit path length. The energy loss per unit path length, dE/dx , is described by the Bethe-Bloch formula [37]

$$\frac{dE}{dx} = 2\pi N_a r_e^2 m_e c^2 \rho \frac{Z}{A} \frac{z^2}{\beta^2} \left[\ln \left(\frac{2m_e \gamma^2 v^2 W_{\max}}{I^2} \right) - 2\beta^2 - \delta - 2\frac{C}{Z} \right] \quad (2.28)$$

where N_a is Avogadro's constant, r_e is the classical electron radius, m_e is the electron mass, ρ is the density of the absorbing material, Z is the atomic number of the absorbing material, A is the relative atomic mass of the absorbing material, z is the incident particle charge in units of e , v the velocity of the incident particle, β is v/c for the incident particle, $\gamma = (1-\beta^2)^{-1/2}$, W_{\max} is the maximum energy transfer in a single collision, I is the mean excitation potential, δ is the density correction and C is the shell correction.

There are two possibilities for the energy loss along the path of a charged particle as it traverses a semiconductor medium: 1) The particle has insufficient energy to pass

through the material 2) The particle does possess sufficient energy to pass through the material.

Alpha particles from Am^{241} passing through GaAs are typical of the first case above. It's dE/dx increases as it loses energy to the medium. After it has travelled a distance in the medium it comes to rest, having lost all its energy to the material. This distance is known as the range and the majority of the lost energy is deposited close to this distance according to the Bragg ionisation curve [37]. The range of Am^{241} in GaAs is approximately 20 μm .

2.5.2 Photons

Semiconductor detectors are commonly used to detect higher energy photons, typically gamma and X-rays. These interact with matter by three basic processes: photoelectric absorption, Compton scattering and pair production. All these processes lead to the partial or complete transfer of the photon energy to electron energy.

In the photoelectric absorption process, a photon undergoes an interaction with an absorber atom in which the photon completely disappears. In its place, an energetic photoelectron is ejected by the atom from one of its bound shells. The interaction is with the atom as a whole and cannot take place with free electrons. The photoelectric process is the predominant mode of interaction for gamma and X-rays of relatively low energy.

Compton scattering takes place between the incident photon and an electron in the absorbing material. It is most often the predominant interaction mechanism for photon energies typical of radioisotope sources. In Compton scattering, the incoming photon is deflected through an angle with respect to its original direction. A portion of energy is transferred from the photon to the electron. Because all angles of scattering are possible, the energy transferred to the electron can vary from zero to a large fraction of the photon energy.

Pair production is possible when the incident photon energy is more than twice the electron rest mass (1.02 MeV). In the interaction, the photon disappears and is replaced by an electron-positron pair. All the excess energy carried in by the photon above the 1.02 MeV required to create the pair goes into kinetic energy shared by the positron and the electron.

Chapter 3

Fabrication Development

3.1 Introduction

The main objective of the work described in this thesis was to develop the technology required to fabricate a 3-D detector. This chapter describes the work done in Glasgow by the author in developing this technology, a brief description of work carried out for the author elsewhere, and the materials used as supplied by the manufacturers.

3.1.1 Material choice

Various types of GaAs substrate material are available worldwide. A common type of substrate material used in the fabrication of radiation detectors is semi-insulating undoped Liquid Encapsulated Czochralski (SI-U LEC). With a resistivity in the order of 10^7 ohm.cm, detectors made from this material possess low leakage currents that are desirable for detector use. This material can be modified if certain wafer characteristics are required, e.g. by In doping, Cr and Fe in-diffusion and low carbon [27] concentrations. Semi-insulating substrate material grown by the Horizontal Bridgman technique [28] is also available, although detectors made from this generally give poorer results than detectors made from SI-U LEC material in our experience [29].

Liquid phase epitaxial (LPE) and vapour phase epitaxial (VPE) materials are available at a greater cost. Low dopant concentrations ($\sim 10^{13}$ cm⁻²) with little charge trapping make these materials desirable for good quality low bias operation. However, the maximum thickness of material of this quality that can be manufactured today (~ 100 μ m) make them a difficult prospect for handling and processing if the substrate on which they were grown is to be removed, as would be required for a 3-D detector.

Currently, the fabrication of a successful 3-D detector is less of a material issue and more of a technology issue; therefore, the more readily available, thicker and less expensive SI-U LEC substrate material was chosen.

3.1.2 Wafer treatment

The wafers used were supplied by Wafer Technology Ltd [30], and were taken from the centre of the ingot where it is believed the material characteristics are most uniform. The wafers arrive unpolished with a diameter of 2 inches and a thickness of 500 μm . They are bought unpolished as we aim to thin and polish them to the desired thickness and surface finish, rendering any manufacturer's polishing unnecessary.

For the creation of a 3-D detector, a wafer approximately 200 μm thick is desirable; this thickness provides sufficient mechanical strength and should enable electrode fabrication to be carried out without difficulty. To achieve this, the wafers were thinned and polished using a Logitech PM4 lapping machine. The wafer was wax bonded onto a flat quartz plate and its thickness measured using a Mitutoyo micrometer. It was then attached by vacuum to a calibrated polishing jig on the PM4, which rotates at a speed of approximately 30 r.p.m. The wafer material is lapped off using this jig combined with a suspension of 3 μm Al_2O_3 particles in de-ionised (DI) water. This process removes about 8 μm per minute from a 2-inch wafer and was used to thin the wafer to approximately 230 μm in thickness.

The next step was to polish both wafer surfaces chemically to a mirror-like "sub-micron" [45] finish using the same machine and jig. This time, a solution of $\text{H}_2\text{O}_2/\text{NH}_4$ with a pH in the range 7.7 - 7.9 was combined with the load to remove the final 30 μm (15 μm per side) of material and polish the surface. Finally, the wafer was de-waxed and cleaned using Opticlear, acetone, methanol and DI water.

3.2 Electrode fabrication

So far, the processing described above is well established and is the same as that used to fabricate a planar detector. It is now necessary to radically deviate from that technology in investigating how to create electrodes that penetrate all the way through a substrate.

To create such an electrode we must first of all create a hole through the substrate. Various possible technologies could be utilised for this, including laser drilling, wet chemical etching and reactive ion etching (RIE). The technology most readily available in Glasgow for creating small diameter holes was laser drilling. This technology has proved successful in drilling holes in GaAs in the past [31].

3.2.1 Laser drilling of holes

The drilling operation was carried out in Glasgow using the Laser Ionisation Group's Nd:YAG laser, which was operated in a repetitively Q-switched mode with individual pulse durations of 10 ns. This laser was chosen due to its small fundamental wavelength (1.064 μm) producing photons with energies that are favourable for drilling small diameter holes. At this wavelength each photon has an energy of 1.16 eV, but if the frequency is doubled to produce a green wavelength of 532 nm then the energy of each photon becomes 2.32 eV. Moreover, the second harmonic frequency has coupling characteristics into GaAs superior to the fundamental frequency. At the shorter wavelengths the absorption depth decreases, the percentage of the beam energy absorbed increases and the energy per photon increases. The combined effects result in orders of magnitude increase in volumetric energy density deposition upon the GaAs from the illumination of the laser beam, compared to what would result from using the fundamental wavelength. Figure 3.1 shows that the absorption depth in GaAs at 532 nm is very small compared to the absorption depth at 1.064 μm [31]. The frequency can be doubled again to produce a wavelength of 266 nm, but there is a practical limit to how many times this can be applied as the frequency doubling process is inefficient and eventually the resultant beam power is too low to be of any use.

To determine which wavelength was the most efficient for drilling, a 150 μm thick GaAs sample was drilled with each subsequent harmonic wavelength using a 15 cm focal length lens. This experiment showed that the third harmonic wavelength of 355 nm was the most efficient wavelength for drilling holes, taking between 30 and 40 pulses to drill through the sample.

The laser-drilling set-up is shown in Fig.3.2. The beam passes through an adjustable iris before being focussed by the objective lens onto the sample. The sample is fixed on an X-Y movable stage that was used to re-position the sample after each hole is

drilled. Various focal length lenses were used, the iris diameter varied and the iris-lens distance varied to see which combination would give the best results. The results of this experiment are described in section 3.2.2.

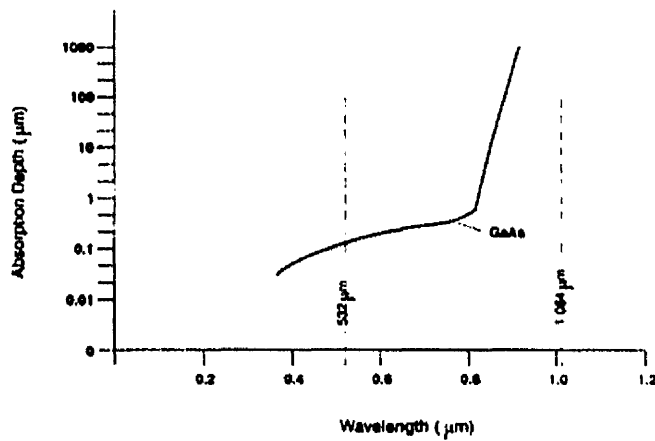


Fig. 3.1 Absorption depth vs wavelength

The equation for the theoretical spot size is [54]

$$s = (4\lambda/\pi)(f/d)M^2 \quad (3.1)$$

where λ = wavelength, f = lens focal length, d = beam diameter entering lens and M^2 is a beam quality factor. When the beam quality factor approaches the theoretical limit of 1.0 (at TEM₀₀) the theoretical spot size equation is reduced to

$$s = 1.27\lambda(f/d) \quad (3.2)$$

It is obvious from this that a shorter wavelength and a short focal length lens will produce a smaller spot size and, consequently, the higher power densities. A larger absorbed power density will result in more effective drilling.

Other tests were made at BNFL using 200 fs pulses from a Ti:Sapphire laser. This set-up benefits from being a fully automatic system with software positional control. The pulse repetition rate was 1 kHz and the wavelength 390 nm. This repetition rate means that each hole can be drilled in less than 0.5 s. The short pulse length of this

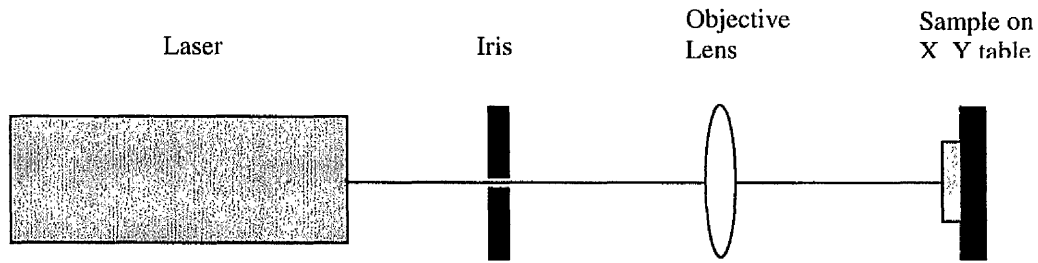


Fig. 3.2 Laser optic path

laser should result in more efficient drilling with less damage to the crystal bulk immediately surrounding the hole.

The distance Y that heat from laser drilling penetrates into the crystal bulk is given by

$$Y = (D_T \tau_p)^{1/2} \quad (3.3)$$

where D_T is the thermal diffusion coefficient and τ_p the laser pulse length. For GaAs, $D_T = 0.24 \text{ cm}^2/\text{s}$. Hence, from Eq. (3.3), the thermal diffusion distance Y equals 2 nm.

The same calculation with the parameters from the Nd:YAG set-up gives a thermal diffusion distance of 500 nm.

3.2.2 Hole Analysis

The holes were analysed using a Philips SEM 515 electron microscope and viewed with Digipad software. The top and bottom surfaces of the hole arrays were observed, with some samples being vertically cleaved to enable the internal walls to be examined. The most significant features of interest were: ejected debris surrounding the hole on the top and bottom surfaces, roundness, repeatability, internal wall surface, taper and cracking.

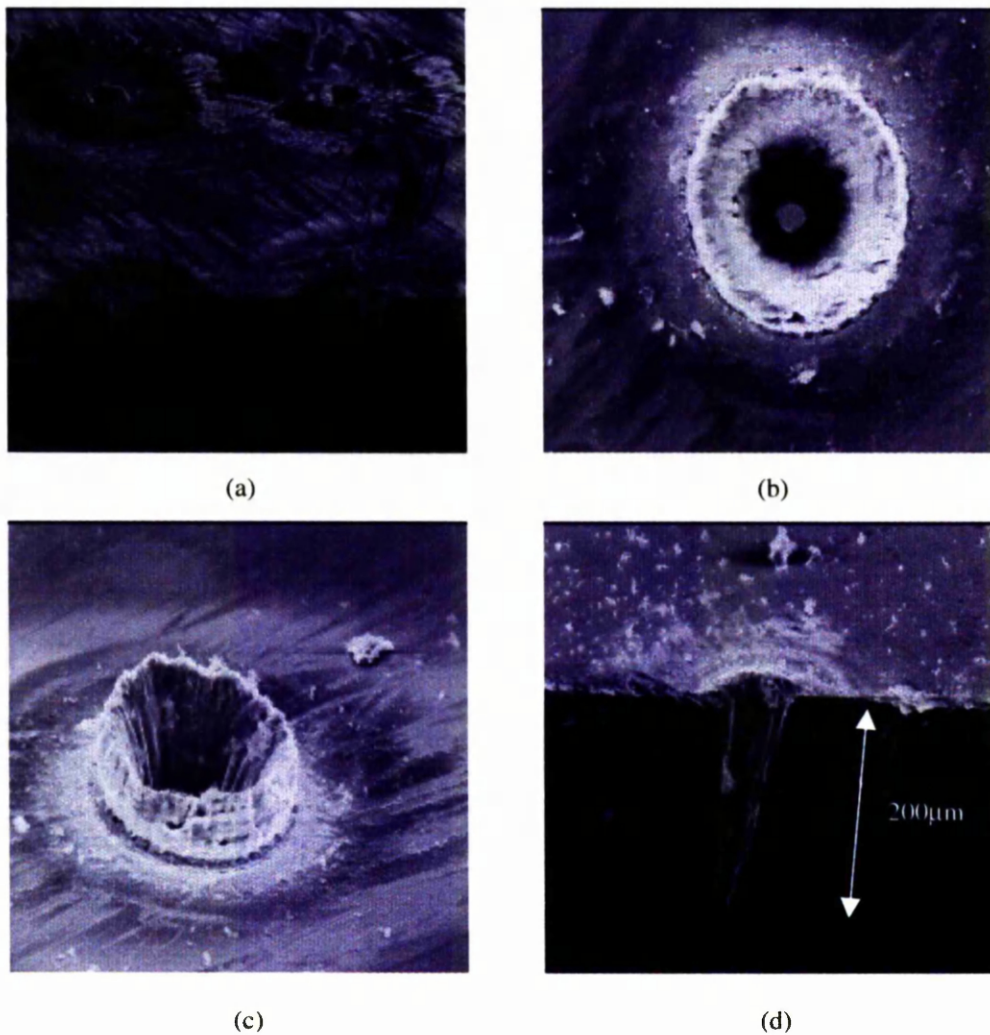


Fig. 3.3 Holes drilled with a 15 cm focal length lens.

Nd:YAG laser

The holes shown in Fig. 3.3a were drilled using a 15 cm focal length lens and an iris diameter of 3 cm. The average power was measured to be 1.5 mW, resulting in 150 μ J per pulse. It took approximately 380 pulses for the laser to drill through the substrate, corresponding to a drilling rate of 0.5 μ m/pulse. Thin film debris has been deposited over a large area surrounding the hole and the cleaved holes show a considerable amount of tapering. Figs 3.3b & 3.3c show a hole viewed from two angles, drilled with the same parameters as above except for the iris diameter, which was reduced to 1mm. It took approximately 590 pulses to drill through, corresponding to a

0.3 $\mu\text{m}/\text{pulse}$ drilling rate. A resolidified wall of ejected molten debris has grown all around the hole. The wall is about 25 μm in height. There is less thin film debris further away from the hole than there is in Fig. 3.3a suggesting that the energy density of the beam has been reduced, which is consistent with Equations 3.1 & 3.2 [54]. The result is that the process is more thermal in nature and the molten debris resolidifies as it leaves the hole. The internal walls show vertical striations that are probably created as the material resolidifies. Figure 3.3d shows a hole drilled similarly to those in Figs. 3.3b & 3.3c. The hole shows a clear tapering effect from top to bottom. The top of the hole is approximately 65 μm in diameter whereas the bottom is around 16 μm , and once again the internal walls show striations throughout the length of the hole. When these holes were drilled the laser was stopped immediately after the exit hole was created.

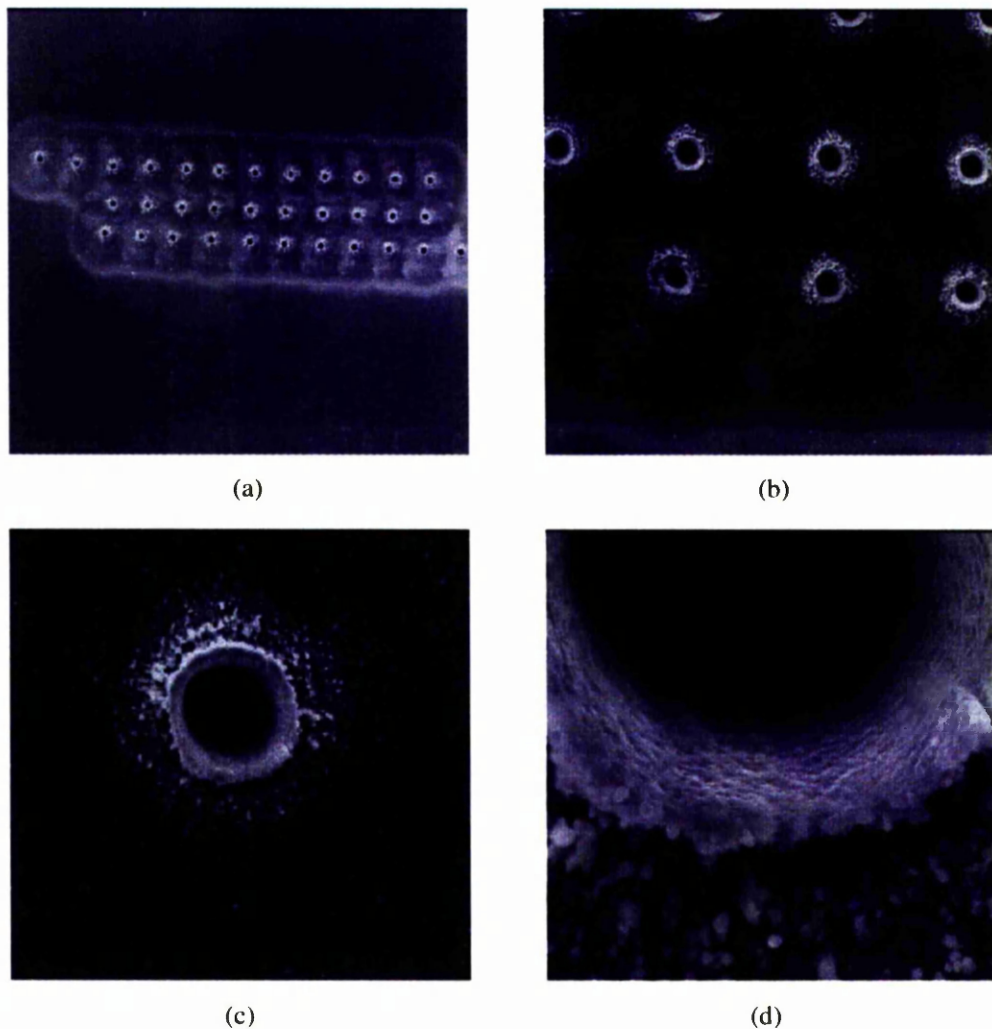


Fig. 3.4 Array of 30 μm diameter holes viewed with increasing magnification from a to d. The holes were drilled with a 5 cm focal length objective lens and an iris diameter of 1 mm.

Figures 3.4a – 3.4d show an array of holes observed with increasing magnification. These were drilled using a 5 cm focal length lens and a 1mm diameter iris.

Approximately 220 pulses were needed to drill through 200 μm of GaAs - a drilling rate of 0.9 $\mu\text{m}/\text{pulse}$. The laser was allowed to run for a further 10 s after the exit hole was created in an attempt to eliminate the tapering effect seen previously. This result will be discussed later. We have achieved a diameter of 30 μm with these parameters as well as an improvement in roundness and repeatability. The debris on the surface shows a resolidified wall as well as a thin film deposition over a larger area that indicates the drilling process operates in both thermal and vapour phases. Finally, the interior walls show a great improvement in smoothness compared to those in Fig. 3.3c. The striations observed with the longer focal length lens have disappeared, with only small pits of about 1 μm in length being observed.

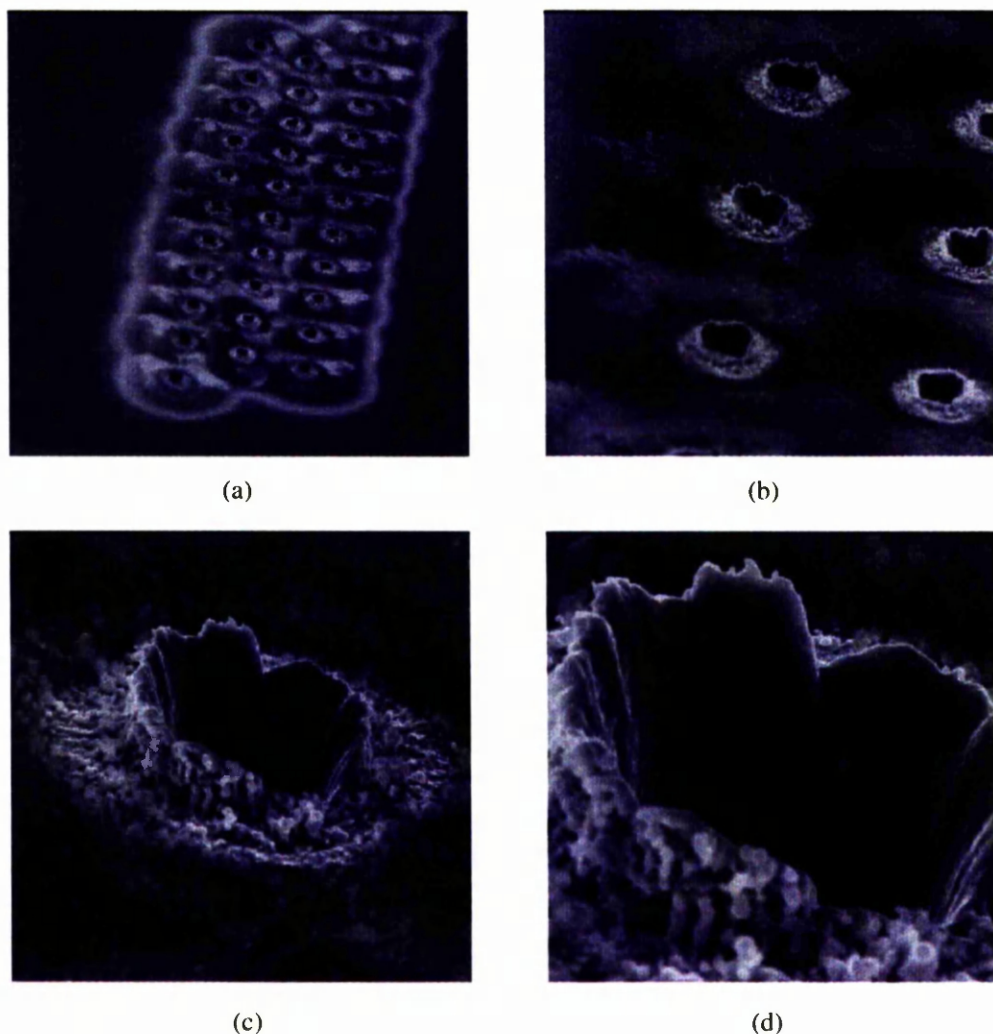


Fig. 3.5 30 μm diameter holes viewed at a 60° angle with increasing magnification from a to d.

Figures 3.5a – 3.5d show the same array of holes viewed from a 60° angle. The smoothness of the internal walls can be seen as well as the height of the resolidified walls. The outer edge of the wall indicates how it was created. Small pieces of molten debris have stuck together forming the wall, suggesting that the debris had been ejected from the hole as small molten pieces.

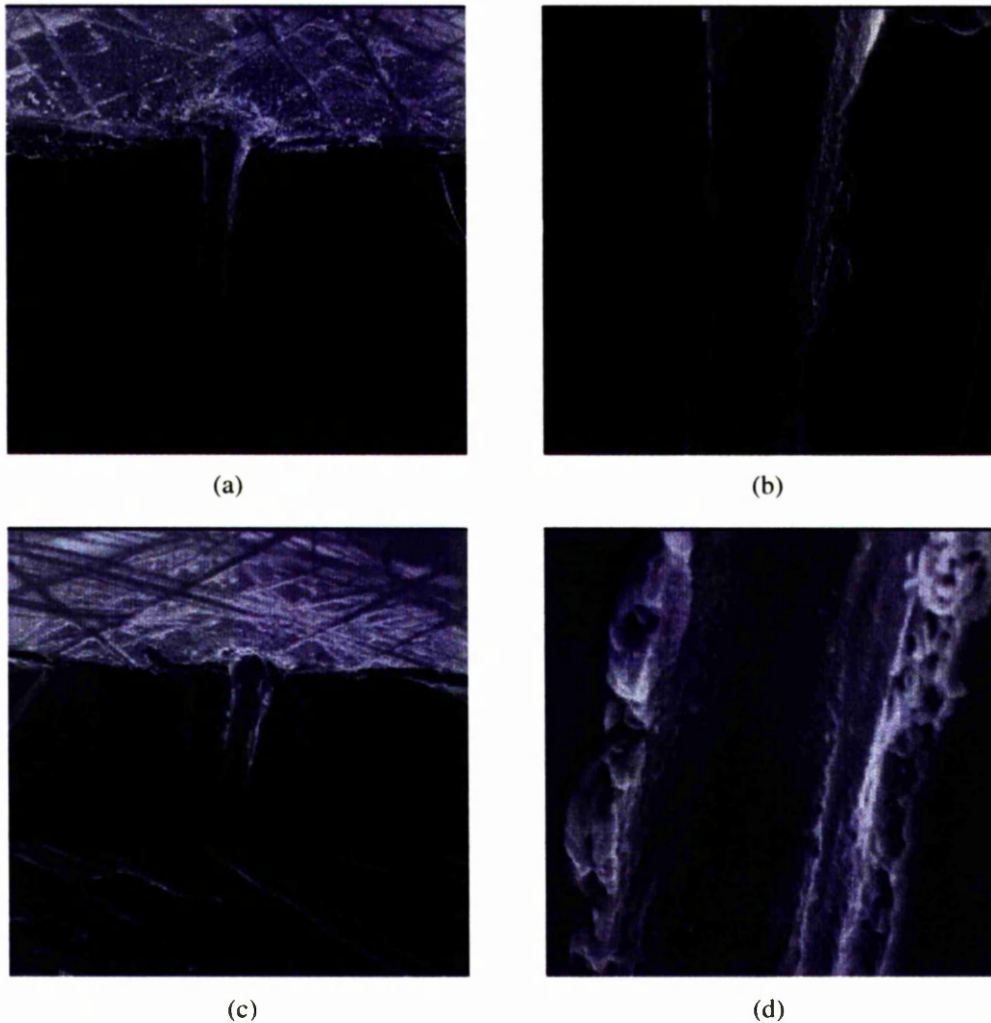


Fig. 3.6 Vertically cleaved holes drilled with a 5 cm focal length lens, 1 mm iris and given an additional 100 pulses after breakthrough.

It was thought that by firing an extra 100 pulses after the exit hole was created, the tapering seen in Fig. 3.3d would be reduced. Figures 3.6a – 3.6d show this reduction. A slight tapering can still be observed in Figs. 3.6a & 3.6b, but there are no signs of tapering at all in Figs. 3.6c & 3.6d. Figures 3.6b & 3.6d show the internal walls, and those exhibit a slightly coarser region near the middle of the bulk, suggesting that this

is a resolidified region. It is possible that the debris being ejected from near the bottom of the hole could not escape completely and created this effect. The internal walls above this region are extremely smooth and show only slight pitting, as seen in previous figures. The ratio of the entry hole diameter to the exit hole diameter gives the degree of tapering over the full length of the hole. The hole in Fig. 3.3c, which was stopped immediately after breakthrough, had a tapering ratio of 4. By running the laser for a further 10 s after breakthrough we have reduced this ratio to very nearly 1.

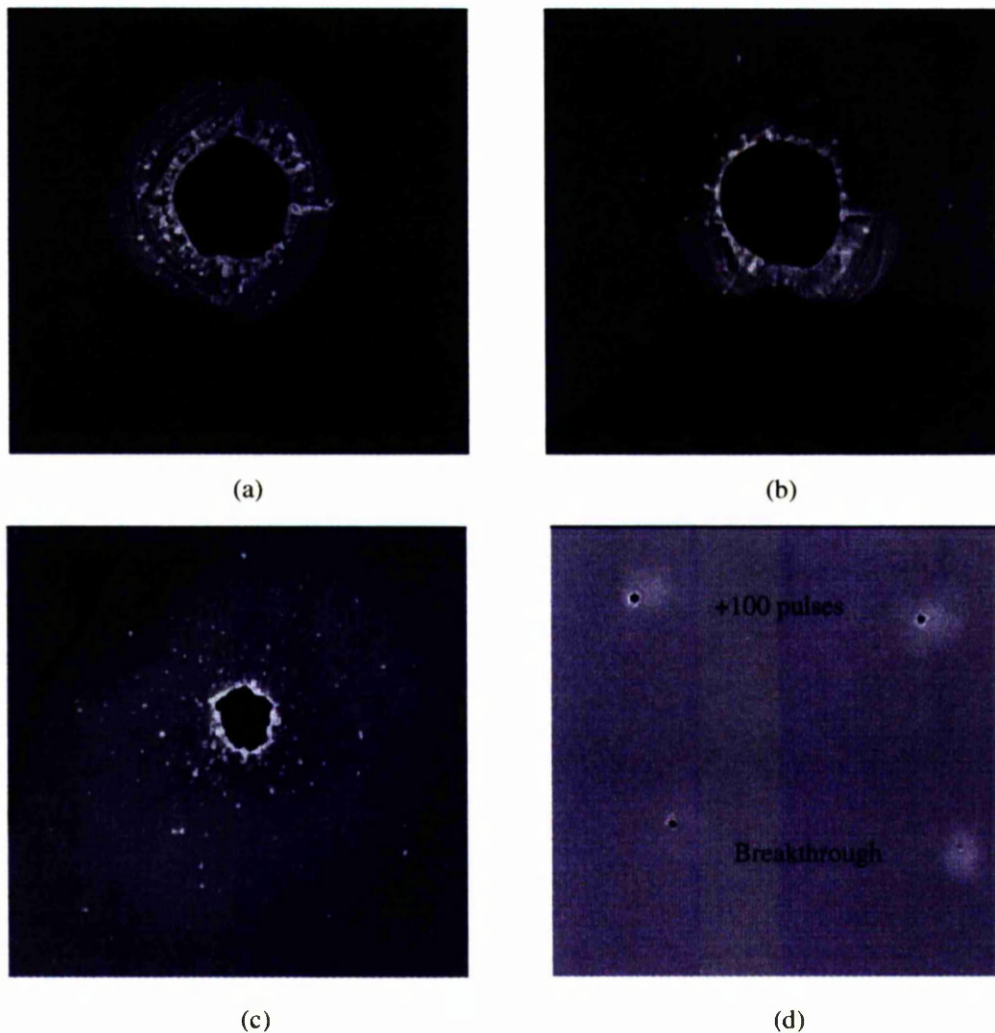


Fig. 3.7 Exit holes on bottom of substrate. (a) & (b) were drilled with a 5 cm focal length lens. (c) was drilled with a 15 cm focal length lens. (d) shows the difference between running for an extra 100 pulses.

Figures 3.7a – 3.7d show exit holes on the bottom of the substrate. The cracks are similar on both Figs. 3.7a & 3.7b. Both holes were created with a 5 cm focal length lens and given an additional 100 pulses after breakthrough. It seems likely that the

energy per pulse is too powerful and these cracks are being created when the exit hole is formed. The views of the internal walls do not show any evidence that these cracks propagate vertically. It could be that they are a localised effect at the exit hole and that a lap and polish would remove the affected area. However, this was not carried out as the problem was not thought to be serious enough to merit further processing at this stage in the development.

Figure 3.7c shows a sample drilled with a 15 cm focal length lens and displays a more erratic circumference. The laser was stopped after breakthrough and it seems likely that the exit hole circumference would have become rounder if additional pulses were fired after breakthrough. Figure 3.7d compares exit holes created immediately after breakthrough with exit holes given a further 100 pulses. The holes were created with a 5 cm focal length lens. The diameter of the exit holes given 100 additional pulses is larger, which is in good agreement with the reduction of the tapering effect seen in Figs. 3.6a – 3.6d. The debris surrounding the holes in all four figures is extremely light in comparison with that displayed on the front of the substrate. Only a thin, final layer or so of material will be expelled from the hole in this direction, resulting in the low level of debris displayed.

Figures 3.8a – 3.8b show a hole drilled with two 5 cm focal length lenses placed 5 mm apart, which created a focal length of 2.5 cm. The hole is approximately 20 μm in diameter but does not display the same roundness as the holes created with the 5 cm lens. This is almost certainly due to the beam profile being distorted by the imprecision of the double lens set-up. The internal walls of this hole show similar pitting to previous holes and the diameter created is consistent with predictions from Eqs. 1&2.

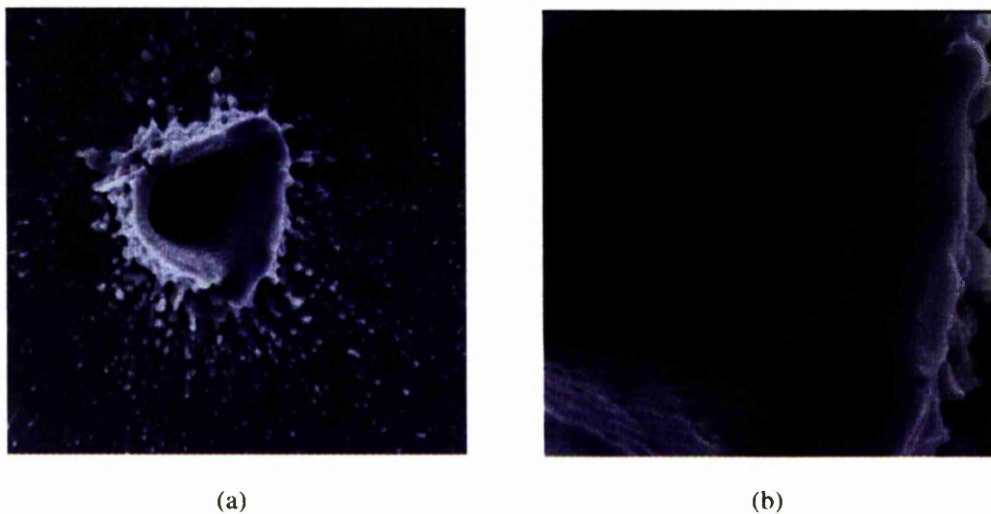


Fig. 3.8 Hole drilled with an effective focal length of 2.5 cm.

Ti:Sapphire laser

Figures 3.9a – 3.9d show holes drilled with BNFL's 200 fs Ti:Sapphire laser. A 15 cm focal length objective lens was used to create a 100 μm diameter light spot. The holes are approximately 100 μm in diameter, which is about 35 μm larger than those drilled with the Nd:YAG laser using the same focal length lens. There is good repeatability and roundness, but the holes differ noticeably from those produced with the Nd:YAG in the lack of debris on the wafer surface immediately surrounding the hole. This is due to the short laser pulse duration, which induces almost complete vaporisation during the drilling process. Consequently, there are no resolidified walls around the entry hole. The internal walls show striations as seen on the first Nd:YAG samples suggesting a narrow heat-affected zone. This may be due to the spot size of the beam, created by the relatively long focal length of the objective lens, rather than any laser parameter. The debris surrounding the hole is light, with no resolidified walls surrounding the holes, as expected with this set-up. Signs of tapering are shown by the difference in diameter of the entry and exit holes, although it must be stressed that this was a feasibility study and not carried out to any specification. The exit holes show extremely erratic circumferences with no repeatability, and the approximate diameter is very much smaller than those of the entry holes, showing that there is also severe tapering. There is no evidence of any cracking around the holes on the back, although we do not have any “complete” holes on which to verify this. Relative to the Glasgow set-up, this laser produces high repetition rate, low energy pulses, which should prevent cracking around the exit hole. As expected, only light layers of debris surround the holes.

Optimum drilling parameters

From this hole drilling feasibility study, the smallest diameter holes obtained that were repeatable, circular, and with little or no tapering, had diameters of 30 μm . These holes were obtained using a 10 ns pulse duration, 355 nm wavelength Nd:YAG laser with a 5 cm focal length lens, 1 mm diameter iris, and by firing the laser for an additional 100 pulses after exit hole breakthrough. All the holes that are referred to later in this thesis were obtained using these parameters.

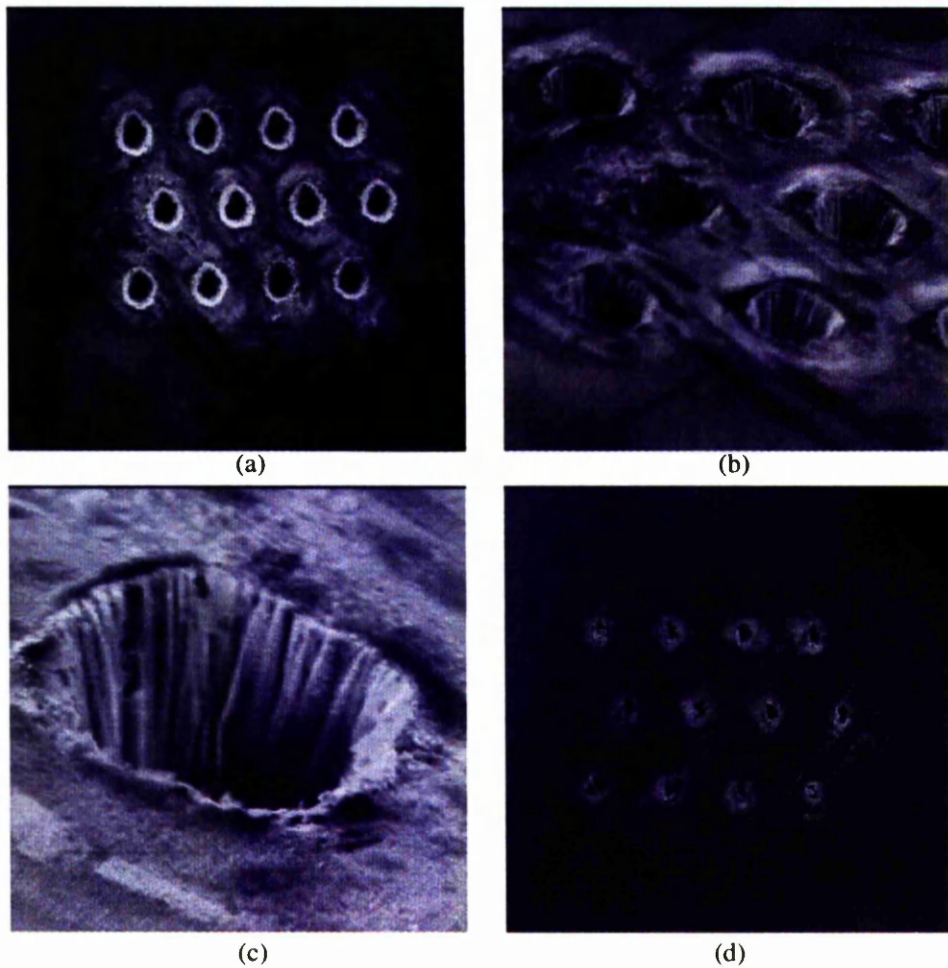


Fig. 3.9 Holes drilled with Ti:Sapphire laser using a 15 cm focal length lens.

3.2.3 Drilling damage

The principal source of surface damage to the wafer undergoing laser drilling is from the debris ejected from the drill hole by the laser. The molten debris that falls on the wafer surface may cause localised melting or may simply stick to the surface. A less serious source of damage is the plasma plume of vaporised material that is expelled from the hole during drilling. This material condenses on any surface around it and forms a thin film on the wafer around the hole.

Various possible processes could be performed to remove this debris or prevent it from sticking to the wafer surface. Current mechanical/chemical polishing procedures, described in section 3.1.2, could remove this debris and recreate a sub μm finish on the surface, although the danger exists that the holes may get clogged up with the

debris as it is being removed. Removal of the debris by etching would be more straightforward as long as the chosen etch does not damage the bulk. An altogether easier way of dealing with this problem would be to prevent it from sticking to the surface in the first place. A protective film that could be removed simply after drilling, e.g. photoresist, spray-on film [31] or silica deposit, would seem to be the easiest solution. The protecting film should be strong enough to withstand the heat transferred from the molten debris, and should be easily removable.

There will be a heat-affected zone immediately behind the internal walls. The thermal diffusion calculations given earlier suggest that heat from the laser will only penetrate $0.5\ \mu\text{m}$ into the substrate, but any damaged region will cause concern regarding the uniformity of the electric field in a biased diode. The holes drilled with the 5 cm focal length lens are very smooth, but do suffer from small-scale pitting. Etching off, say, $1\ \mu\text{m}$ of material from the internal walls would remove any damaged material, and leave a relatively smooth surface on which to fabricate the electrodes. A p-type selective etch would be best, as it is likely that the material on the interior wall surface will be gallium-rich, the arsenic having evaporated due to sublimation. Also, stoichiometric GaAs beyond the heat affected zone would not be etched with this etch.

The cracking at the exit hole is probably caused by the energy of the laser pulses being too high. A possible improvement could come from a higher repetition rate, lower laser pulse energy, which would break through the final layers less vigorously. In the absence of this equipment, a mechanical/chemical polish would remove the damaged material, only if the damage does not penetrate deeply into the substrate.

Given that we have now developed the technology to create round, repeatable holes in which to form electrodes, we will now attempt to prevent or remove any causes of drilling damage to the substrate and then attempt to form electrodes within these holes.

3.2.4 Resist spinning

The first step is to prevent the molten and vaporised material, ejected from the hole during drilling, from being deposited around the hole on the substrate. The simplest method available is to spin photoresist across the substrate before drilling. This layer of resist has three functions:

- 1) Protect the wafer surface from the debris ejected from the hole during drilling.
- 2) Protect the wafer surface from any etch used to treat the internal walls of the holes.
- 3) Protect the wafer surface from any metallisation process used to create electrodes within the holes.

A wafer sample, described in sections 3.1.1 & 3.1.2, was cleaned on both sides in an ultrasonic bath according to the following procedure:

Opticlear (10 mins); Acetone (5 mins); Methanol (3 mins); Reverse Osmosis (RO) water (rinse).

Opticlear, an organic terpene, is used to remove any wax remaining from the lap and polish process, and acetone removes any human grease from the surface. Methanol prevents any remaining acetone from evaporating quickly, which can leave dirt particles on the wafer surface, and rinsing with RO water removes any remaining methanol. The wafer is then dried with a compressed nitrogen flow.

Through a 0.45 μm filter, the photoresist was applied in small drops to provide a uniform film across the sample. The sample was then spun on a Headway Research Inc. spinner at 1000 rpm, creating a film with a thickness of approximately 5 μm . The sample was then baked in an oven at 90^o C., to evaporate the solvent in the photoresist, leaving behind a hard film. Both top and bottom faces of the substrate need this protection, so it was necessary to carry out the above procedure on both sides.

Holes approximately 30 μm in diameter were then drilled in the sample using the optimised parameters described previously.

3.2.5 Wet chemical etching

The heat from the laser drilling process will damage the GaAs crystal in the region immediately behind the walls of the holes. This heat-affected zone will have a degrading effect on any diode and should therefore be removed.

The layer of photoresist used to protect the wafer surface from ejected debris also lends itself to removing the heat-affected zone by wet chemical etching. The internal

walls can be etched away using a GaAs etch, while the photoresist protects the substrate surfaces from its effects.

The GaAs etchant used was a sulphuric acid: hydrogen peroxide: RO water solution in a ratio of 1:8:40[32], which has an etch rate of approximately 5 $\mu\text{m}/\text{min}$. According to Equation (3.3), the heat-affected zone will penetrate 0.5 μm into the substrate and should therefore only need to be immersed in this etch for 6 s. With the subsequent metal evaporation process in mind, it was decided to immerse the sample in the etchant for 2.5 mins to create a 60 μm diameter hole. A large diameter hole would give a better chance of creating a metal contact throughout the full length of the hole.

3.2.6 Metal Deposition

The next step in creating a 3-D diode is to form the electrodes within the holes. Various options have been attempted in the past, including metal evaporation and electro-plating [33]. Metal evaporation is a versatile method, as a number of metals can be readily evaporated and evaporation facilities were readily available.

Before metal evaporation, the sample was de-oxidised for 30 s in a 1:1 solution of ammonia and RO water. This removed any oxide that had grown on the internal walls since the drilling process.

The metal deposition was carried out using a Plassys MEB 450 evaporator. This evaporator contains an electron beam cannon and a rotating crucible with a choice of six metals within the vacuum chamber. Recipes can be formulated using any of the six available metals with any thickness up to approximately 300 nm.

The recipe chosen to create the electrode consisted of: 33 nm titanium; 30 nm palladium; 150 nm gold. The titanium layer creates a Schottky barrier on the GaAs substrate. The palladium layer acts as a barrier to the gold, which could otherwise diffuse rapidly through the titanium into the substrate, and the relatively thick layer of gold facilitates wire bonding for electrical characterisation. This recipe has been used extensively in the past for fabricating planar diodes [34]. Results show that Schottky barrier diodes with leakage currents below 100 nA are consistently obtained

The evaporation is carried out by focussing a 10 kV electron beam onto a metal disc at a pressure of approximately 10^{-7} bar. The heat from the beam tears atoms from the metal disc and projects them towards the sample where they are deposited. This process is carried out in turn for each chosen metal.

It was not obvious that evaporating from one side would form a contact throughout the full length of the holes in the sample, since evaporated metal atoms tend to stick to the first surface they collide with. Accordingly, the sample was evaporated from both sides to maximise the possibility that the evaporated metal from both sides would extend as far as the middle of the hole. At the time of writing, it was not possible to cleave this sample and check if this was successful. However, any electrical tests should provide an indication as to the success of this process.

After both evaporations, the sample was soaked in acetone to remove the photoresist on both surfaces of the sample. Metal from the evaporations, along with debris from the drilling process that was sitting on top of the photoresist, was washed away when the acetone was removed. Agitation from an ultrasonic bath helped with this removal. Subsequent cleaning of the sample with methanol and RO water prevented any dirt particles from the acetone being deposited on the sample. The sample was then dried with compressed nitrogen.

3.2.7 Wire Bonding

The final step in creating the detector was to attach wires to each electrode to enable the detector to be characterised electrically. To do this, a length of 25 μm diameter aluminium bond wire with a drop of silver-loaded conducting epoxy adhesive on the tip was manually inserted into each hole. The adhesive fills the top of the hole, and when cured makes an electrical connection between the wire and the gold-covered electrode. The other end of the wire can be easily attached to a solder pad, enabling connection to electrical equipment.

3.2.8 Fabrication Summary

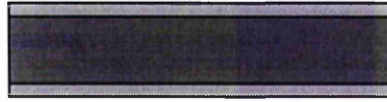
Figure 3.10 shows the complete process flow to fabricate a 3-D detector.

1. The GaAs sample was thinned down to the required thickness using mechanical lapping and chemical polishing. The sample was then cleaned with Opticlear, acetone, methanol and RO water to remove any wax and dirt from the sample.
2. Resist was spun on both sides to protect the sample surface from subsequent processing.
3. Holes were drilled through the sample using a 10 ns pulse duration, 355 nm wavelength Nd:YAG laser with a 5 cm focal length lens, 1 mm iris, and by firing the laser for an additional 100 pulses after exit hole breakthrough.
4. The internal walls were etched with a solution of sulphuric acid, hydrogen peroxide and RO water to remove the heat-affected zone from the substrate.
5. The Schottky contact was formed by evaporation of Ti/Pd/Au (33/30/150 nm) from both sides of the sample.
6. The photoresist on both surfaces was removed using acetone in an ultrasonic bath. The sample was then cleaned with methanol and RO water.
7. Al wire tipped with a silver-loaded epoxy adhesive was inserted into the holes to form electrical connections.

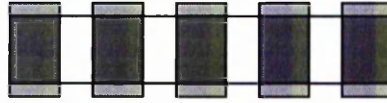
1) Lap and polishing
Cleaning procedure



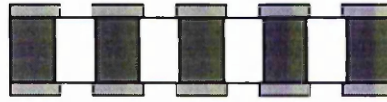
2) Resist spinning



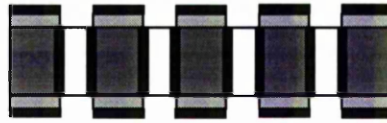
3) Hole drilling



4) Wet etching



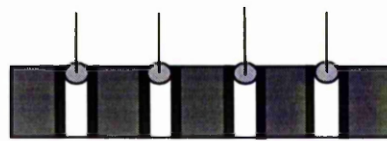
5) Metal evaporation



6) Resist stripping
Cleaning procedure



7) Wire bonding



Chapter 4

Detector characterisation

4.1 Introduction

Following the development of the processing technology and the device fabrication of a 3-D detector, the electrical and charge collection characteristics of the device were investigated. These characteristics are fundamental in obtaining an understanding of the device and deciding on any future developments. To this end, computer simulations of this type of detector with various dimensions were also carried out. The author carried out the electrical and charge collection tests in the Detector Development Group laboratory at the University of Glasgow. The simulations were carried out in the same laboratory in conjunction with the author.

4.2 Current-voltage characteristics

A Keithley 237 source measurement unit was used to measure the dependence of the current through the device with applied bias. A LabView [35] program was written to control the Keithley via a GPIB interface, enabling the results to be written into a spreadsheet. The detector was fitted inside a metal box, providing the device with RF electrical and light shielding. The measurements were carried out in a Heraeus environmental chamber, which can control temperature to an accuracy of 0.2°C between -40°C and 160°C . This temperature control was very important as the current characteristics are temperature dependent. All measurements were made from zero initial bias. A voltage step was applied and the current measured after a 10 s delay. The delay allowed any current fluctuations to settle. A current limit was set to prevent the flow of currents above $1\ \mu\text{A}$, which could be damaging to both the device and measuring equipment.

4.2.1 Three-electrode cell

The first sample tested was a three-electrode cell. Figure 4.1 shows the circuit used in this measurement. The three electrodes are of the Schottky type, so all measurements were taken with a Schottky-Schottky configuration (in planar detectors it is more common to have a Schottky-Ohmic configuration). The central electrode was biased, both forward and reverse, while the other two electrodes were held at ground. The electrodes in this cell were $60\ \mu\text{m}$ in diameter with a $210\ \mu\text{m}$ pitch.

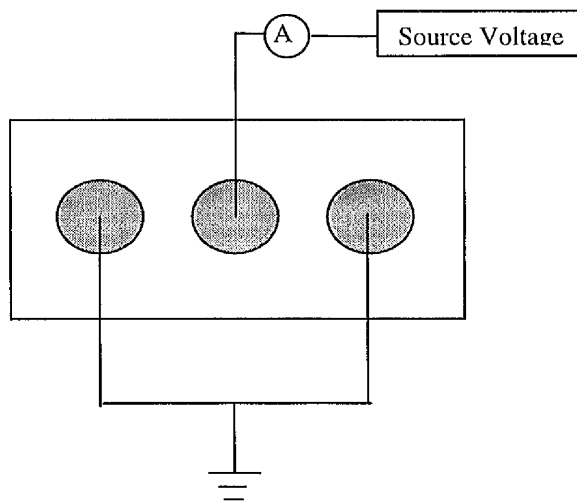


Fig. 4.1 Three-electrode test circuit.

The forward and reverse bias characteristics are shown in Fig. 4.2. The first and most reassuring feature is that the cell shows familiar reverse biased diode characteristics; a relatively stable reverse bias leakage current region up to a certain bias ($\sim 100\ \text{V}$) followed by a sharp breakdown region beyond this value.

The next notable feature is that the forward and reverse bias characteristics are asymmetrical, unlike a planar diode with two identical Schottky electrodes, which has symmetrical forward and reverse characteristics. This effect is understandable due to the asymmetric nature of the cell structure; two grounded electrodes flank one biased electrode. Therefore, when the central electrode is forward biased, reverse biased Schottky barriers will be created on both the outer electrodes, whereas only the central electrode will support a Schottky barrier when it is reverse biased. This creates a

greater active surface area when the cell is forward biased, resulting in an increased leakage current. The structure has no guard ring and therefore surface states will increase the leakage current [36]. This effect is directly proportional to the surface area. The forward region characteristic also shows a “softer” current increase compared to the sharp breakdown in the reverse region.

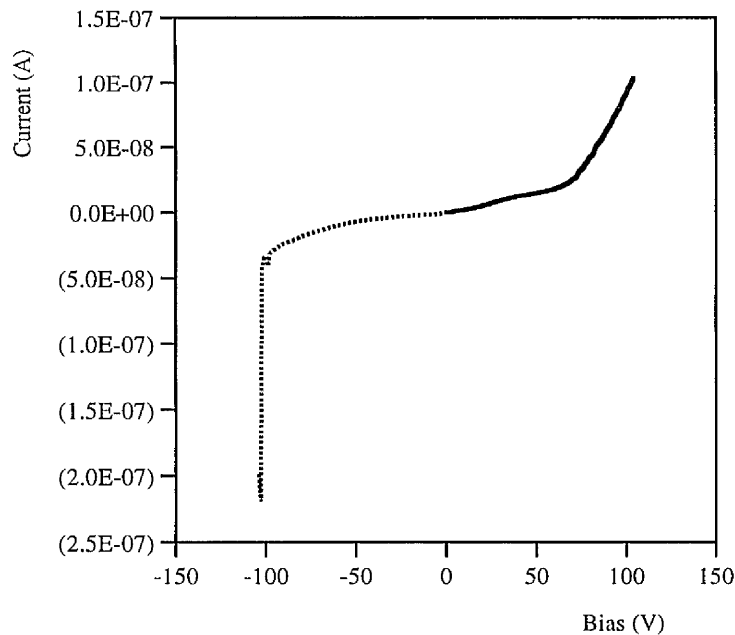


Fig. 4.2 Three-electrode cell I-V characteristics.

Figure 4.3 shows the reverse region in greater detail. The leakage current magnitude is relatively low (below 50 nA) but isn't as stable as the leakage current seen in a guarded planar diode. However, at this magnitude it is not a significant problem. The breakdown voltage in the reverse region is approximately 100 V.

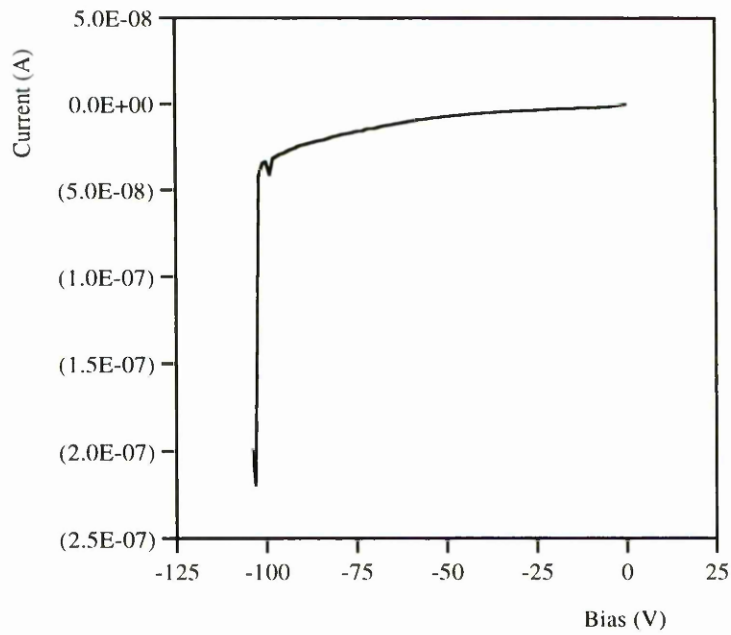


Fig. 4.3 Three-electrode cell reverse bias characteristic.

4.2.2 Nine-electrode cell

Figure 4.4 shows the circuit used to measure a nine-electrode cell. In a multiple cell array this would constitute an individual cell. The central electrode is biased while the surrounding eight electrodes are held at ground. The dimensions and diode configuration are the same as those in the three-electrode cell.

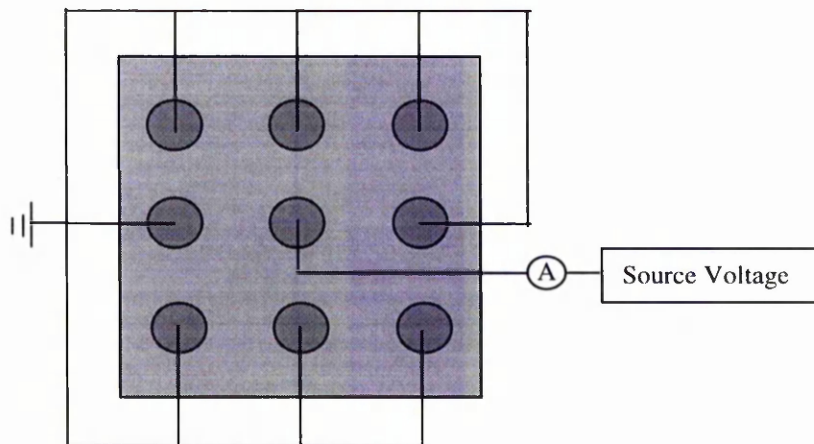


Fig. 4.4 Nine-electrode cell test circuit.

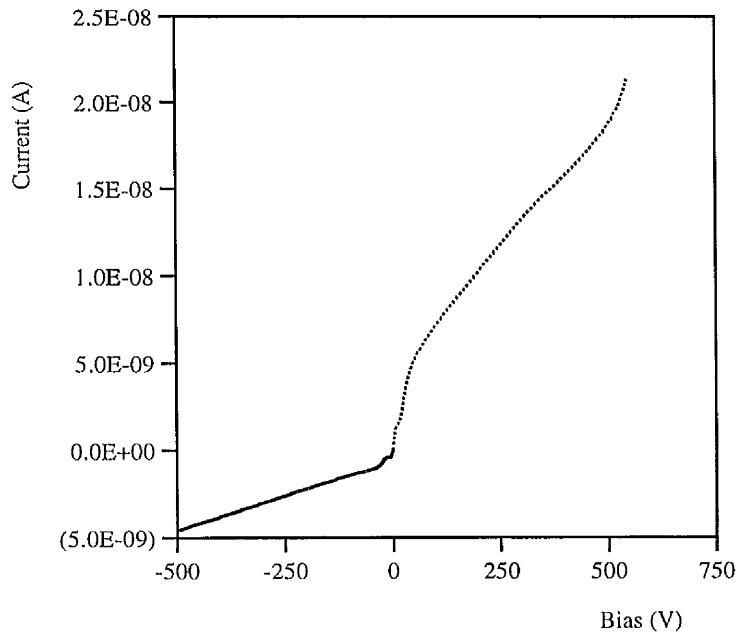


Fig. 4.5 Nine electrode cell I-V characteristics.

Figure 4.5 shows the forward and reverse characteristics for the nine-electrode cell. It was possible to apply a far greater bias to this cell than to the three-electrode cell – 500V was applied in both directions before the device broke down. The high value of breakdown voltage could be attributed to the electric flux density surrounding each electrode. The drift lines are spread almost equally from the central electrode to the eight surrounding electrodes, creating a less dense electric field region at each electrode than that of a three-cell device. Breakdown occurs more readily in a contact region of high electric field density due to charge injection from that contact. Figures 4.6a and 4.6b show this effect. The density of drift lines surrounding the outer electrodes in Fig. 4.6a is less than that in Fig. 4.6b, resulting in the three-electrode cell in Fig. 4.6b breaking down at a lower applied bias. There is also the possibility that a large series resistance existed between the bondwire and electrode, with a consequent voltage drop across it. This resistance could have been caused by the creation of poor quality Schottky barriers in the holes – the unpolished GaAs surface on which the electrodes were formed would not have the “sub-micron” finish that the polished wafer surfaces possess – or from poor contact adhesion from the conducting epoxy glue. It was not possible to verify this by testing another cell, as there was only one cell available.

The characteristics for this cell are even more asymmetrical than those for the three-electrode cell. Both forward and reverse characteristics show leakage currents below 20 nA and breakdown voltages of approximately 500 V. The reverse characteristic in particular shows a very flat leakage current plateau up to approximately 500 V before abruptly breaking down. The increase in current here was so great that the compliance mechanism on the Keithley could not record it. This breakdown could be due to avalanche breakdown as a result of impact ionisation caused by the high electric field. Charge injection from the eight surrounding electrodes could contribute to this breakdown but the detector would have to be fully depleted for this to happen. The magnitude of the leakage current at 500 V is 5 nA. The forward characteristic leakage current magnitude is approximately 20 nA at 500 V. Although this is four times greater than the reverse characteristic, it is still a very low value for this value of applied bias. It is possible that this low leakage current was due to the multiple electrodes creating a guarding effect on the active device area, keeping surface states to a minimum and resulting in a low leakage current. The three-electrode cell has a higher leakage current at a lower applied bias, which is consistent with this theory.

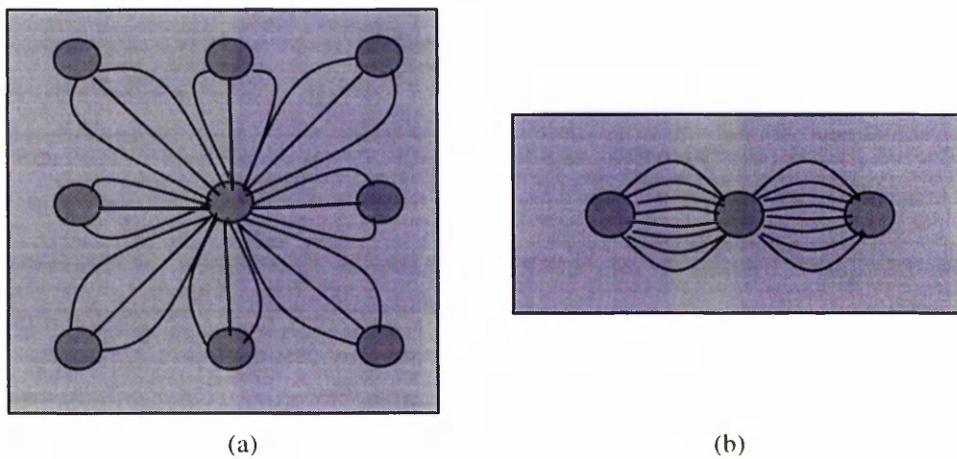


Fig. 4.6 Approximate electric flux density for (a) 9 electrode cell (b) 3 electrode cell.

4.3 Charge Collection

The 3-D cells have been measured and characterised with respect to their electrical properties. The next feature of interest is their ability to function as ionising radiation detectors. If charge signals can be obtained from these cells then the basis for further development of the devices will be in place.

The measurement of charge collection efficiency as a function of applied bias is the most informative test for a radiation detector. This measurement can be carried out with alpha, beta and gamma illumination. Each type of illumination deposits its energy in different ways within the crystal and therefore gives different information about the detector performance. For example, in planar detectors an alpha source test allows the electron and hole charge collection to be investigated individually [34,46], whereas measurements made with minimum ionising particles (from a beta source) allow the charge collection of both carriers across the entire bulk of the detector to be calculated. For this investigation however, these finer details are of less importance than simply obtaining a signal from the device. Any spectrum that is separated from the noise will be regarded as a success and a platform for future investigations.

4.3.1 Alpha particle tests

The apparatus used for the alpha measurements is shown in Fig. 4.7. The detector was tested with both forward and reverse bias on the central electrode via an EG&G Ortec 142 charge pre-amplifier. The surrounding electrodes were held at ground. The device was placed inside an RF screened box - for electrical and light screening - which had a hole drilled through one side. An Americium - 241 source placed above this hole irradiated the device sitting just below it with 5.45 MeV alpha particles.

Alpha particles have a limited range in air due to their heavy mass and large cross-section, and so the RF box was placed inside an evacuated metal container at a pressure between 20 and 30 mbar. Signals from the device were read out via the pre-amplifier, through a post amplifier with a 500 ns shaping time, and processed by a PC-based multichannel analyser (MCA) to obtain a pulse height spectrum.

A calibration of the MCA was performed for each amplifier gain setting in order to calibrate the ADC channels in the MCA in units of charge. A voltage pulse was applied to a 1.8 pF capacitor connected to the front end of the pre-amplifier.

The charge induced in the capacitor can be calculated by:

$$Q_{in} = V_p C_t \quad (4.1)$$

where Q_{in} is the accumulated charge in the capacitor, V_p is the amplitude of the voltage pulse and C_t the value of the capacitor.

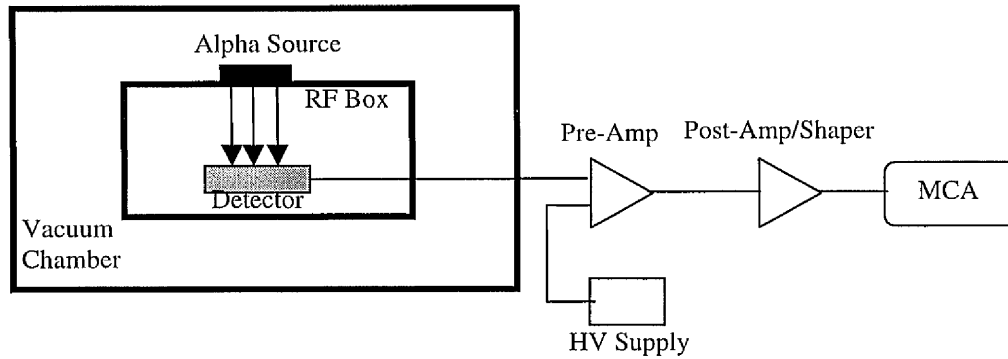


Fig. 4.7 Alpha source test measurement apparatus.

In GaAs, alpha particles deposit energy according to the Bragg ionisation curve [37], which results in most of the alpha particle energy being deposited at a depth of approximately 20 μm below the surface. We can calculate the amount of charge liberated by the total absorption of these alpha particles. This is found to be:

$$Q_{tot} = \frac{E_a}{\varepsilon} = \frac{5.45\text{MeV}}{4.27\text{eV}} = 1.274 \times 10^6 e^- \quad (4.2)$$

where ε is the energy needed to create an e-h pair in GaAs [38]. The charge collection efficiency (CCE) is defined as the ratio of the charge measured by the detector, Q_m , divided by the total charge liberated by the incoming radiation, Q_t , i.e.

$$CCE(\%) = \frac{Q_m}{Q_t} \times 100\% \quad (4.3)$$

The GaAs material used in the fabrication of the 3-D cells contains both electron and hole traps [38,39]. Therefore, the charge carriers may not be able to cross the

thickness of the detector between electrodes without being trapped, leading to the carriers having a mean free absorption length less than this thickness. Ramo's theorem [6,7] states that the charge induced, Q_{col} , on the electrodes of a detector by the motion of a charge carrier is given by:

$$Q_{col} = q \frac{\lambda}{W} \quad (4.4)$$

where λ is the mean free absorption distance travelled by the carrier and W is the distance between the detector electrodes. Charge carrier trapping will reduce the number of free carriers with distance of detector traversed (x) according to the exponential relationship:

$$n_x = n_0 \exp\left[-\frac{x}{\lambda}\right] \quad (4.5)$$

where n_0 is the original number of carriers produced. The charge collection efficiency is therefore:

$$CCE = \frac{\lambda}{W} \left(1 - \exp\left[-\frac{W}{\lambda}\right]\right) \times 100\% \quad (4.6)$$

Taking into account the signal from both carriers we get:

$$CCE = \frac{\lambda_e}{W} \left(1 - \exp\left[-\frac{(W - x_0)}{\lambda_e}\right]\right) + \frac{\lambda_h}{W} \left(1 - \exp\left[-\frac{x_0}{\lambda_h}\right]\right) \times 100\% \quad (4.7)$$

where x_0 is the position at which the carriers were created.

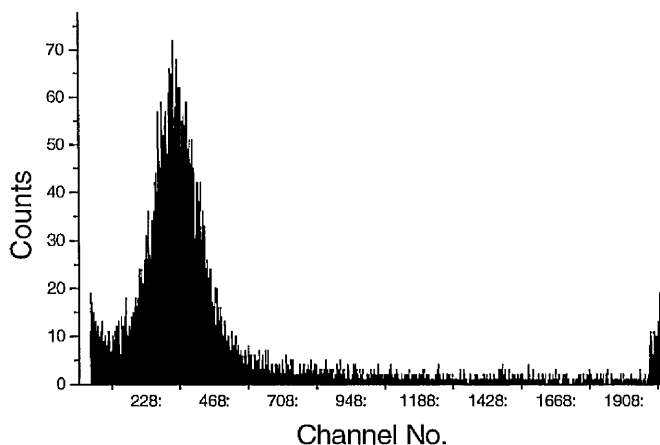


Fig. 4.8 5.45 Mev α particle spectrum of nine electrode cell at room temperature.

Figure 4.8 shows the spectrum obtained using an Am^{241} source at an applied bias of 300 V at room temperature. The spectrum is clearly separated from the noise pedestal and shows the familiar Gaussian shape of an alpha spectrum obtained from a planar diode. For this device, both types of charge carrier will contribute to the total charge collected, but it is impossible to tell by how much as there is no “front “ or “back” on this device (for planar devices, the contribution from each carrier can be calculated by illumination from both sides of the device). From the position of the Gaussian distribution in the spectrum, the CCE can be determined using Eq. 4.3. The CCE for this spectrum was calculated to be 48%. The rate of counting is very low compared to standard planar diodes, with the peak channel displaying approximately 70 counts compared to many hundreds or thousands for a planar diode.

A Gaussian curve was fitted to the above spectrum to obtain the full width at half maximum (FWHM). From this value the signal-to-noise (S/N) ratio can be obtained. The S/N ratio for the above spectrum was measured as 3:1. This is a poor ratio and was probably due to a combination of poor quality electrode-bulk interfaces and a noisy alpha source [53]. Tests on planar diodes [25] have shown the importance that good quality electrode-bulk interfaces have on detector performance.

The CCE measurements as a function of applied bias are shown in Fig. 4.9. The maximum CCE in this plot is 50%. This incomplete charge collection is a

manifestation of charge trapping, which affects both types of charge carriers and is seen in planar diodes made from the same material. The curve is flat, with the CCE at 100 V applied bias, only 12% below that at 450 V applied bias.

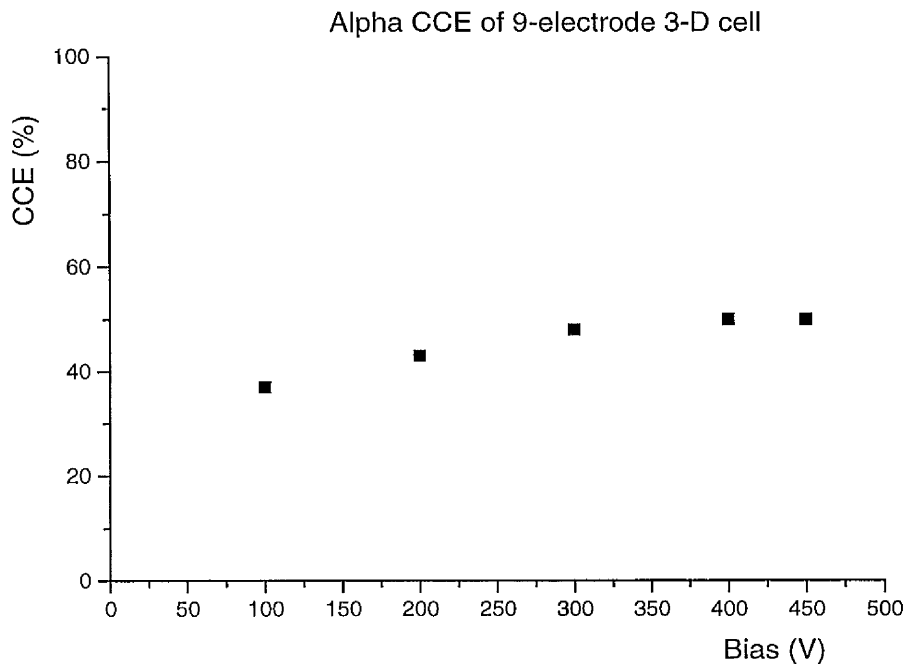


Fig. 4.9 CCE measurements of 5.45 MeV α particles at room temperature.

4.3.2 Gamma source tests

At an energy of 5.45 MeV, and the fact that they deposit all of their energy within 20 μm of material, alpha particles are the source of radiation that is easiest to detect using GaAs. It was interesting to see if the 3-D cell could detect much lower energy radiation with a lower specific energy loss. For this purpose, a 60 keV gamma source was used to test the cell using the same apparatus as that for the alpha tests.

As expected, it proved very difficult to obtain a spectrum from this source, and at biases up to 400 V it was not possible to separate the signal from the noise. However, at 450 V bias a spectrum was eventually obtained. Figure 10 shows this spectrum.

The count rate is extremely low (only 12 counts at the peak channel) but enough to show a recognisable spectrum separated from the background noise.

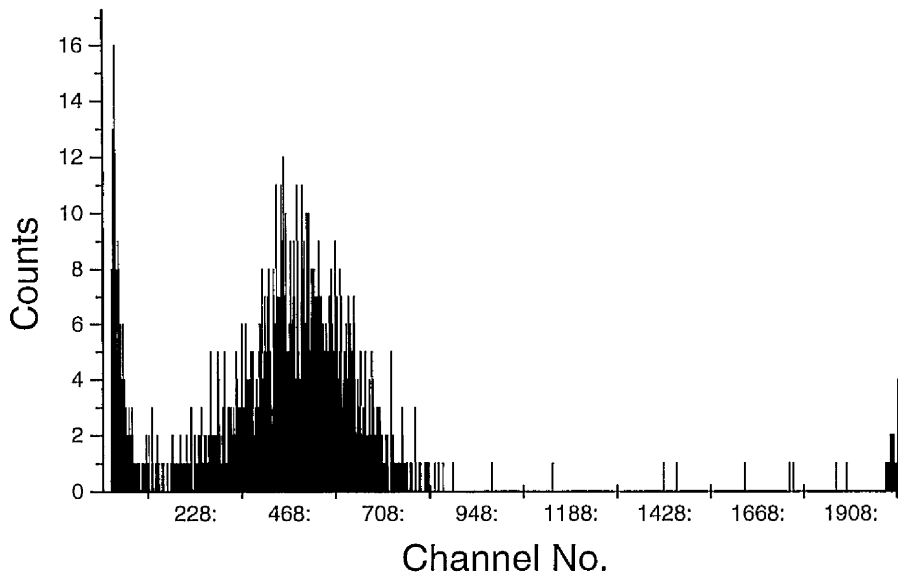


Fig. 4.10 60 keV γ -ray spectrum of nine electrode cell at room temperature.

4.4 Simulated performance

Electrical characteristics were calculated using the MEDICI software package [51], a powerful simulation program that can be used to simulate the behaviour of semiconductor devices. The program solves Poisson's equation and both the electron and hole current continuity equations to analyse devices such as diodes.

Such calculations offer two main benefits:

- 1) Provide a theoretical prediction that can be validated by experimental results. Experimentally unmeasurable parameters can also be inferred.